Utrecht University

MSc THESIS

Solute transport in porous media; An experimental pore-scale study using physical micromodels

Author:
Bernadette Raaijmakers

Supervisor: dr. A. Raoof
Co-supervisor: Enno de Vries MSc

A Thesis submitted in fulfilment of the requirements
for the degree of MSc Hydrology

Earth Surface and Water
Hydrogeology
Department of Earth Sciences
Utrecht University, the Netherlands

July 9th, 2018

Abstract

Groundwater contamination is a worldwide problem and is predominantly caused by soluble contaminant compounds in the aqueous phase. Therefore, it is essential to understand transport of contaminants in groundwater bodies. For that reason, dispersion of solutes in saturated porous media has been the subject of many studies. However, saturated porous media lacks experimental data to provide more insight in the porosity and flow rate dependency of hydrodynamic dispersion. This study aims to research the effects of porosity and flow rate on dispersion in single-phase flow and transport in porous media. By injecting an ink solution in micromodels with varying porosity (n = 0.435, 0.494, and 0.551) and under various flowrates (Q = 0.05, 0.1, and 0.2 ml hr^{-1}) solute transport was recorded real-time using an optic visualization setup. By determining the relation between the image grayscale intensity and ink concentration value in the micromodel, solute breakthrough curves (BTCs) were obtained. Next, the BTCs were analysed using the analytical solutions to obtain estimates of longitudinal dispersivity (α_L). An increase in porosity was found to decrease dispersion and therefore decrease the longitudinal dispersivity. An increase in flow rate was found to increase mixing of the solute in the saturated micromodel, leading to an increase in α_L. One two-phase flow experiment was carried out, which proves that similar mechanisms can be researched under two-phase conditions with the fabricated heterogeneous porous network and visualization setup.

Contents

List of Figures

List of Tables

List of Symbols

Symbol	*Description*	*Unit*
α_L	Longitudinal dispersivity	L
μ	Fluid viscosity	$ML^{-1}T^{-1}$
σ	Interfacial tension	MT^{-2}
a	Fitted constant in relation between concentration and grayscale intensity	[-]
A	Cross sectional area	L^2
b	Fitted constant in relation between concentration and grayscale intensity	[-]
C	Concentration	ML^{-3}
$C^{t}_{i,j}$	Pixel neighbourhood concentration at time t at location ij	[-]
d	Characteristic length	L
D_e	Effective diffusion coefficient	L^2T^{-1}
D_L	Longitudinal dispersion coefficient	L^2T^{-1}
I^t_{ij}	Neighbourhood grayscale intensity value at time t at location ij	[-]
L	Length of domain	L
n	Porosity	[-]
N_c	Capillary number	[-]
Pe	Péclet number	[-]
PV	Pore volume	[-]
Q	Total discharge	M^3T^{-1}
t	Time	T
t_r	Hydraulic residence time	[-]
u	Pore velocity	LT^{-1}
v	Average flow velocity	LT^{-1}
x	Distance	M

1 Introduction

Groundwater contamination is a well-known global problem with an ever increasing population diminishing natural water resources. Groundwater contamination is largely caused by soluble contaminant compounds dissolved in the aqueous phase (Korom, 1992; Corapcioglu et al., 1997). Global population growth over the last few decades has caused an increase in food and drinking water demand, resulting in increasing groundwater pollution and scarcity (Vörösmarty et al., 2000; Vitousek et al., 1997). This results in a growing interest in the transport processes of agricultural chemicals such as pesticides and fertilizers, but also that of pharmaceuticals and personal care products (PPCPs) transported from the vadose zone to groundwater and soil systems, which poses a threat to nature and quality of groundwater supplies (Nielsen et al., 1986; Dahan, 2016; Zentner et al., 2015). Therefore, it becomes increasingly important to understand the behaviour of contaminants in groundwater bodies. To comprehend large scale phenomena such as groundwater contamination, it is essential to understand what takes place on pore scale, e.g. how contaminants compounds are transported and solutes disperse through porous medium.

Migration of fertilizers and solutes in vadose zone is controlled by various multiscale physical and chemical processes. When reaching the water table, solute migration develops under single-fluid conditions. Solute transport in porous media is primarily controlled by dispersion, advection and diffusion and is different under single-fluid conditions compared to multifluid (i.e. multiphase) conditions, as in unsaturated porous media (Karadimitriou et al., 2016). To model dispersion of groundwater and soil contamination of the processes stated above, it is necessary to have a reliable estimate of dispersivity.

1.1 Saturated flow transport principles

Dispersion is caused by the different flow paths of water particles, which leads to mechanical mixing and a diluted solution in the groundwater system. For hydrodynamic dispersion, Fick's law is used to connect dispersion to the concentration gradient. An equation commonly used to describe conservative solute transport in a homogeneous porous medium is the advection and dispersion equation (ADE) (Bear & Cheng, 2010):

$$\frac{\partial C}{\partial t} = D_L \frac{\partial^2 C}{\partial x^2} - u \frac{\partial C}{\partial x} \qquad (1)$$

where $\partial C/\partial t$ is the change in solute concentration over time [MT^{-1}], C the solute concentration [ML^{-3}], D_L the longitudinal dispersion coefficient in the x-direction [L^2T^{-1}], x the distance [L] and u the pore velocity [LT^{-1}].

The longitudinal dispersion coefficient, D_L [L^2T^{-1}], is a linear function of average velocity and saturation degree of the porous medium. Under saturated conditions it is defined by (Bear, 1988):

$$D_L = D_e + a_L v \qquad (2)$$

with D_e as the effective diffusion coefficient of the medium [L^2T^{-1}], α_L longitudinal dispersivity [L] and v the average flow velocity [LT^{-1}]. In most cases concerning flow in saturated porous media, the effect of diffusion in transport of solutes is negligible, as the typical velocity in aquifers ranges from 1 cm day^{-1} to 1 m day^{-1} (Hassanizadeh, 2016). Longitudinal dispersivity is considered to be a function of soil property for saturated flow (Raoof & Hassanizadeh, 2013). It characterizes the dispersion of solutes transported by fluids flowing through porous media (Xu & Eckstein, 1997). It is scale-dependent, and dispersivity values of less than 1 mm to more than 1 cm are reported

for laboratory columns. An empirical relationship for longitudinal dispersivity is given by the following approximation (Hassanizadeh, 2016):

$$\alpha_L = 0.0175\sqrt{L^3} \quad (3)$$

Where L [L] the length of the domain of interest represents. Many factors have an influence on dispersivity such as particle shape and flow velocity, however the main influences are effective grain size and uniformity coefficient. Xu & Eckstein (1997) show that dispersivity increases with effective grain size and porosity on field scale and in laboratory columns (Xu & Eckstein, 1997).

The relative effect of advection compared to molecular diffusion can be quantified by the Péclet number. As dispersion is linearly related to advection, the Péclet number is also an indicator of the influence of dispersion over diffusion (Freeze & Cherry, 1979).

$$Pe = \frac{vd}{D_e} \quad (4)$$

With Pe representing the Péclet number [-], v as the average flow velocity [LT^{-1}], d as the characteristic length [L], representing the average particle diameter, and D_e as the effective diffusion coefficient of the medium [$L^2\,T^{-1}$].

1.2 Unsaturated flow transport principles

Velocity distribution and transport phenomena are altered when the wetting saturation in porous media decreases (Jiménez-Martínez et al., 2015). It creates preferential pathways of wetting fluids with a high flow velocity, but also regions with trapped wetting fluids, the so-called immobile zone (Karadimitriou et al., 2016). Immobile zones cannot contribute to solute transport by advection and solute transport in these zones will only take place by diffusion, in contrast to the mobile zones. This transport characteristic of flowing and stagnant zones created by the degree of saturation and the two fluid interaction leads to a larger dispersion coefficient compared to saturated (single fluid-phase) conditions and an increase in dispersion, with a decrease in saturation (e.g. Raoof & Hassanizadeh, 2013). In two phase flow in porous media, the displacement of one phase by another in the pores is caused by capillary pressure, defined as the difference between the pressure of the non-wetting phase and the pressure of the wetting phase across the interface. Capillary forces emerge from the interfacial tension between two phases and a curvature caused by the phase distribution within the pore network (Cense & Berg, 2009). During multiphase flow in porous media, the capillary entry pressure has to be exceeded for the non-wetting fluid to infiltrate a wetting fluid-filled pore throat. The non-wetting fluid can only penetrate small pores if the capillary pressure is great enough to bend the interface between the nonwetting and wetting fluid sharply enough to make it fit through the entrance of the pore (Fitts, 2012).

1.3 Literature review on micromodels

Karadimitriou & Hassanizadeh (2012) define a micromodel as an idealized representation of a porous medium, usually in two dimensions. It is a structure of connected pores, on a scale of microns, through which it allows fluids to flow and solutes to disperse (Karadimitriou & Hassanizadeh, 2012). The pores in the model are extremely small (< mm), otherwise capillary

effects would become irrelevant (Karadimitriou, 2013).

Chatenever and Calhoun (1952) created one of the first micromodels to examine microscopic mechanisms of fluid behaviour in porous media. Since then, micromodels have been used for various research purposes such as colloid transport and remobilization (Wan & Wilson, 1994; Zhang et al., 2013; Zhang et al., 2015), viscous and capillary fingering (Lenormand et al., 1988), solute transport (Corapcioglu & Fedirchuk, 1998) and enhanced oil recovery (Lifton, 2016; Sayegh & Fischer, 2008). In the biomedical field micromodels have been used for monitoring and controlling symptoms, cell manipulation and drug delivery (Perestrelo et al., 2015; Zhao, 2013) and big advances have been made with Organ-on-a-Chip and Body-on-a-Chip microfluidic devices (Huh et al., 2010; Caplin et al., 2015). A relatively new research area in soil science is the use of micromodels for solute transport in unsaturated conditions. Important progress has been made in research of solute transport under single phase conditions in porous media, however the effect of saturation on solute dispersion and transport is still under discussion (Karadimitriou et al., 2016; Jiménez-Martínez et al., 2017). Using transparent micromodels with an irregular pore network will make it possible to gain knowledge of pore scale level processes in the saturated zone.

1.4 Objective

Our objective was to quantify flow rate and porosity dependent solute dispersivity on pore scale level by developing physical micromodels with an irregular porous network of 10 by 10 mm and to use them to carry out saturated solute transport experiments. The following steps were carried out in order to understand the fluid flow and solute transport through the porous medium.

Three micromodels with varying porosity but similar pore structure were prepared to carry out solute transport experiments. The experiments have been carried out under similar conditions but with varying flowrates (Q = 0.05, 0.1, and 0.2 ml hr^{-1}). Ink-water solution was injected in each micromodel saturated with water, at three different flowrates. For the same micromodels and flowrates, water was injected in order to flush the micromodels while they were saturated with an ink-water solution. This resulted in total in 18 different sets of images. Real-time images of these experiments have been recorded by a high resolution camera. They are analysed using MATLAB software (The MathWorks Inc., 2018) to obtain solute breakthrough curves (BTCs). The resulting breakthrough curves are fitted using the analytical model CXTFIT (Toride et al., 1995), used for solute transport in porous media using analytical solutions of the ADE to obtain relevant transport parameters. Further results include analysed real-time images of the saturated experiments and concentration maps of the porous network. To research the possibility of using micromodels to study the same mechanisms with two-phase flow, one two-phase flow experiment is carried out. The images of this experiment are included in the results, but were not further analysed.

By obtaining the above results, this aim of the study is to provide insight in the effect of varying flow rate and porosity on solute dispersivity under saturated conditions.

2 Materials and Methods

2.1 Experimental setup

The experiments were carried out at the Porous Media lab at the GML (Gemeenschappelijk Milieu Laboratorium) of Utrecht University. Figure 2.1 shows a schematic of the experimental setup, which is essentially an open-air microscope. On the left of the figure, a high precision syringe pump (Harvard Apparatus, Pico plus Elite 11) is shown, carrying a Hamilton 1000 5 ml syringe (no. 1). Syringes containing ink, water or Fluorinert were placed into the pump and connected to the PDMS micromodel (no. 2).

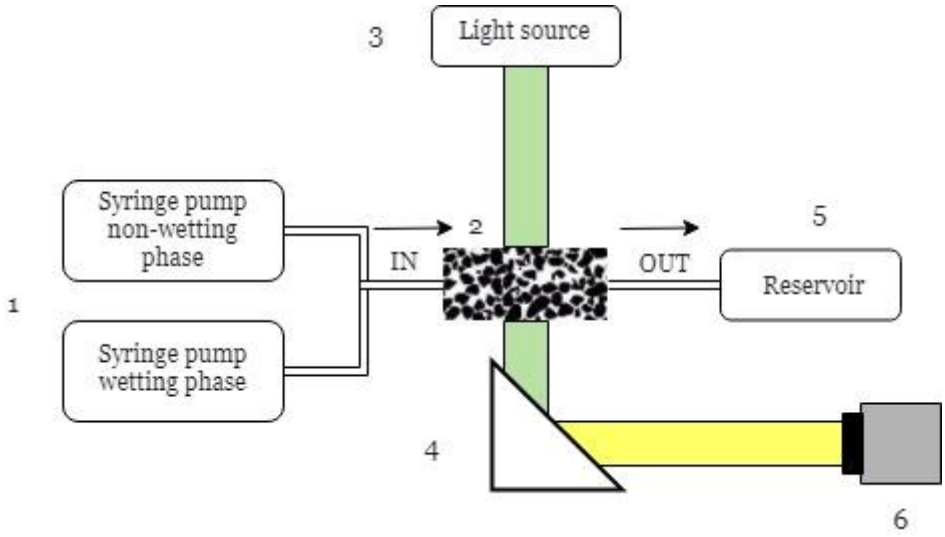

Figure 2.1 Schematic of experimental setup, numbers indicating the various components

The micromodels were illuminated by an orange LED light source which emitted light at a wavelength of 590-610 nm (no. 3), levelled straight above the model. A prism was put underneath the micromodels (Edmund Optics) (no. 4). The camera, a Canon EOS 5DSR with 180mm f/3.5 macro lens (no. 6), was placed so it could capture dispersion occurring within the microchannels. In order to shoot RAW images, the camera captured images at a speed of 0.2 fps. To avoid any vibrations caused by the camera or other sources, it was placed at a short distance from the micromodel. The setup was placed on a vibration isolation table to prevent the experiment being affected by any external vibrations. The fluids were collected in a reservoir, attached to the outlet of the micromodel (no. 5). The images were processed and stored on a desktop computer. Due to the use of a single camera, the micromodels were treated as a 2-D porous medium. All experiments were conducted under the same conditions, e.g. constant room temperature, pressure, and constant LED-lighting.

2.2 Micromodel

2.2.1 Micromodel fabrication

The micromodels were made of polydimethylsiloxane (PDMS), a silicon-based elastomeric material. PDMS is widely used for the fabrication of microfluidic devices due to the fact that they are relatively cheap to make and safe and easy to use in a laboratory environment (Karadimitriou et al., 2013). Using a micromodel in this research gave the advantages of exactly controlling the

pore space and grain distribution. The procedure of manufacturing a PDMS micromodel is briefly explained here, a more elaborate description can be found in Karadimitriou et al. (2013).

The micromodel was composed of two PDMS slabs, one containing the pore network and the other functioning as a blank cover. The pore network was designed and printed on a transparent fused silica blank, which is used as a mask. The mask was used to create a patterned wafer; it was spin-coated with negative photoresist (SU-8 2025, MicroChem) and by using photo-lithography, a pattern was created on a silica wafer. The wafer was put in a vacuum chamber and salinized, to prevent the photoresist features to be peeled of along with the PDMS. PDMS is made with a silicon elastomer base (Sylgard 184, Dow Corning) and its accompanying elastomer curing agent . It was mixed at a mass ratio of 10:1, which corresponds usually to 50 g of the base and 5 g of the curing agent. To remove air bubbles which were trapped in the PDMS due to the mixing, the mixture was put into a vacuum chamber. After degassing the mixture, the wafer was put in a petri dish and PDMS was poured over it. Another petri dish was prepared with PDMS only, to create the layer to seal off the micromodel. The petri dishes were placed in the vacuum chamber, again to degas the PDMS from trapped air bubbles. The PDMS was cured in an oven for at least two hours at 68° degrees Celsius and carefully peeled from the master. The PDMS slabs were covered with tape to prevent contamination of the samples. In the inlet and outlet of the slab containing the pore network holes were punctured, to provide access to the network.

There are various methods to connect two slabs of PDMS to each other, resulting in different wettabilities. The PDMS slabs for this research were bonded to each other by exposing them to a corona discharge. After exposure, the two slabs were pressed together for bonding. To achieve complete bonding, the micromodels were placed in an oven at 68° degrees Celsius to cure for a few hours. To create a stable uniformly hydrophobic surface, the micromodels were treated after the corona discharge with a silane solution (Karadimitriou et al., 2013).

2.2.2 Wettability issues

For flow experiments, it is important that the micromodels have a uniform and stable wettability. PDMS of itself is hydrophobic with a water contact angle >100°, but is not uniformly distributed (Karadimitriou et al., 2013; Mata et al., 2005). As a result of the bonding process of the PDMS slabs, the wettability of the micromodel is altered. When using a corona discharge, PDMS is made more hydrophobic than its original state. However, due to atmospheric exposure, it eventually returns to its natural state of non-uniform hydrophobicity. By introducing a silane solution into the micromodel, the micromodel was made uniformly and stable hydrophobic. As the micromodels were hydrophobic, water could not be the wetting fluid. Therefore in this research, water was the non-wetting fluid as well as the ink-water solution. In the two-phase flow experiment, Fluorinert acted as the wetting fluid. Fluorinert (FC-43) is a clear non-flammable and non-toxic fluid with a liquid density of 1860 kg m^{-3}, a viscosity of $4.7x10^{-3}$ Pa.s and a solubility in water of <5 ppmw. The interfacial tension between water and Fluorinert is 58 mN m^{-1} (3M, 2000).

2.2.3 Pore network

In this study, three different pore networks were used. All three networks had an similar grain distribution, connectivity and consist of a network of 10 x 10 x 0.069 mm; only the size of the grains varied, resulting in varying porosity and average grain size diameter. The models are shown in Appendix A. The porosity of the micromodels was respectively 43.5% (model 1), 49.4% (model 2), and 55.1% (model 3), with the corresponding average grain size diameter and other characteristics outlined in table 2.1 The pore network was based on a computed tomography (CT) scan of a slice of natural sand packed soil. To create models with varying

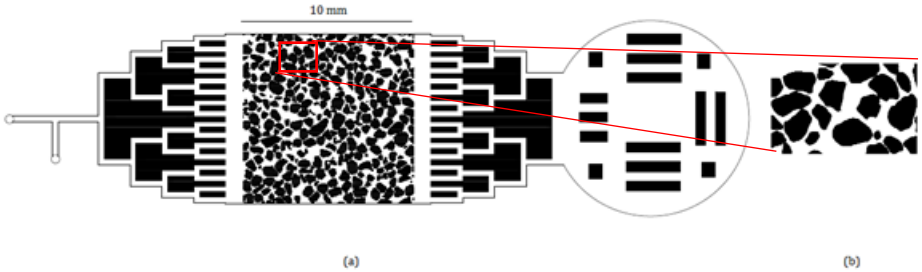

Figure 2.2 (a) Image of model 1 with inlet on the left side and outlet on the right. The void space is shown in white, and grains in black. (b) Zoomed-in image of a part of the pore network

porosity but similar pore structure, the grains in the network of the original pore network were eroded. This caused for some of the small grains to disappear when eroding the grains, resulting in smaller number of grains with an increasing porosity (table 2.1).

An inlet and outlet structure are implemented to create an uniform introduction of the solute in the porous network. They were designed in such a way that the pillar structure adds support to the inlet and outlet, preventing it from collapsing. By spatially analysing the pore network in MATLAB (The MathWorks, Inc. (2018)), the average diameter of the grains of the porous media were calculated. The average grain diameter was used in order to calculate the Péclet number.

Table 2.1 Porous network characteristics

	Porosity [-]	**Average grain diameter [mm]**	**Number of grains**
Model 1	0.435	0.477	311
Model 2	0.494	0.450	310
Model 3	0.551	0.437	297

2.3 Experimental method

2.3.1 Micromodel and setup preparation

The micromodels used in the experiments are described in Section 2.2. Preparation of the micromodels and setup is outlined in a few steps below. It was essential for the model to be as clean as possible, including no fibres or residue left in and on the micromodels. This was to avoid pixel contamination of the images, which could lead to an overestimation of the solute concentration. The model was cleaned with industrial lens cleaning towelettes (ProWorks) and fiber optical cleaner (Edmund Optics). Even though the models were cleaned as good as possible, it was nearly impossible to fully clean the models of all contaminants. After many attempts, there seemed to be no clear method on how to clean PDMS models as efficiently as possible. Therefore, some residue was left on the model. To carry out the experiments, it was required that all parts of the setup were levelled. If not, the micromodel would show significant shadows along the grains and other edges which is shown in Figure 2.3 a. After levelling the setup, the camera settings were set to give the best possible images. To minimize vibrations and to obtain in focus images, the images were captured with a fast shutter speed and low aperture. The ISO was kept low to minimize noise in the images. The LED light was controlled by a power supply control (Tenma).

Testing has been done to find the best light conditions for the experiments. After preparing the setup, the micromodel was put underneath the LED source and secured to prevent movement of the model. Due to the hydrophobic nature of the micromodel, water would not naturally displace air trapped in the model during the saturated experiment. To ensure all air would be displaced by the injected water, the model was flushed with sufficient CO_2-gas for a few minutes. CO_2-gas dissolved in water and the model reached full saturation.

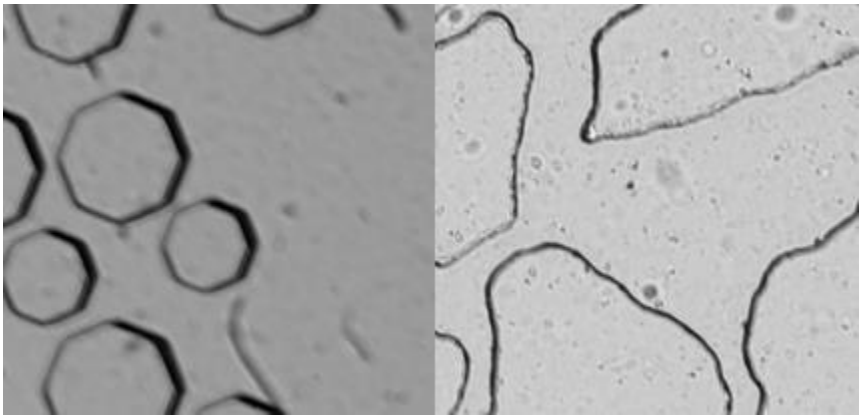

Figure 2.3 On the left a close up of a micromodel at the beginning of the research with significant shadows, on the right a close up of model 1 after accurate levelling of the setup

2.3.2 Concentration and grayscale values

The flow experiments were carried out with blue ink (578 cyan, Ecoline). To be able to detect concentration differences in the images, the ink had to be diluted first to a solution of 25% water and 75% ink. This solution will be called from now on as the *ink solution*. If the ink was not diluted in the first place, the ink spreading through the porous medium would be too dark to notice any concentration differences and therefore would not be suited to analyse.

To be able to identify the relation between concentration value and grayscale intensity value from the RAW images, initial experiments were carried out. Five known concentrations were prepared for the initial experiment and diluted a second time with water. This resulted in the solutions outlined in Table 2.2.

Table 2.2 Five known solutions used for the initial experiment

0%	Only water
25%	25 % ink solution, 75% water
50%	50 % ink solution, 50 % water
75%	75% ink solution, 25 % water
100%	Only ink solution

The solutions with known concentration values were introduced in the micromodel before each flow experiment. Grayscale values were determined for the pixels by taking images of the models whilst saturated with the known solution. Knowing the concentration of the solute and the accompanying grayscale value, a correlation between the two values was found. According to the Beer-Lambert law, the relation between the pixel intensity of the image and the known concentration is an exponential function, with the intensity of the pixel decreasing exponentially with the concentration of the ink (Kohl et al., 2006). After several trials, we concluded that the ink should not be diluted too much in order to maintain the relationship between pixel intensity and concentration. If the ink solution is diluted to a greater extent, e.g. 80% water and 20% ink, the

relation between pixel intensity and concentration became nearly linear (see App. B). The correlation we found between pixel intensity and concentration resembles previous research (e.g. Kohl et al., 2006).

The scale of light intensity captured by the camera varied between 1, which represents a completely black pixel, and 255, which represents a completely white pixel. The ideal situation would have been if a certain concentration would corresponds to only one intensity value. However in practice it turned out that a concentration corresponded to a small range of pixel intensity levels, which can be observed in the histograms shown in Appendix B. The range in intensity level is due to the fact that not all ink particles absorb and emit the exact same amount of light, causing a variance in intensity levels, which is reflected in the histograms as a spread in pixel intensity. Therefore, in order to properly analyse the images, a median grayscale pixel intensity of 15-by-15 pixels neighbourhoods of the pore space was calculated. The use of averaging neighbourhoods can be compared to a median filter; any anomalies in pixel intensity left in the images are averaged out as well. Not all neighbourhoods consisted of 225 pixels, therefore neighbourhoods with less than 20% of the original amount of pixels were merged with a neighbourhood adjacent to it.

For the micromodels, a unique relation was identified which fits the measurements of the corresponding experiment with a coefficient of determination accuracy of over 99%. For every neighbourhood block of 15 by 15 pixels, the relation between concentration and grayscale value was found to be:

$$C_{i,j}^{t} = ae^{bI_{i,j}^{t}} \qquad (5)$$

With $C_{i,j}^{t}$ as the concentration value of the 15x15 pixel neighbourhood at time *t* and at location *ij*, *a* and *b* as fitted constants, unique for each micromodel, and $I_{i,j}^{t}$ as the grayscale intensity value of that block. Table 2.3 shows the average values for *a* and *b* found for each micromodel, figure 2.4 shows the grayscale value plotted versus concentration. Histograms and median values of the micromodels showing the relation between ink concentration and grayscale intensity can be found in Appendix C.

	a	b
Model 1	1.60	-0.033
Model 2	1.58	-0.031
Model 3	1.53	-0.032

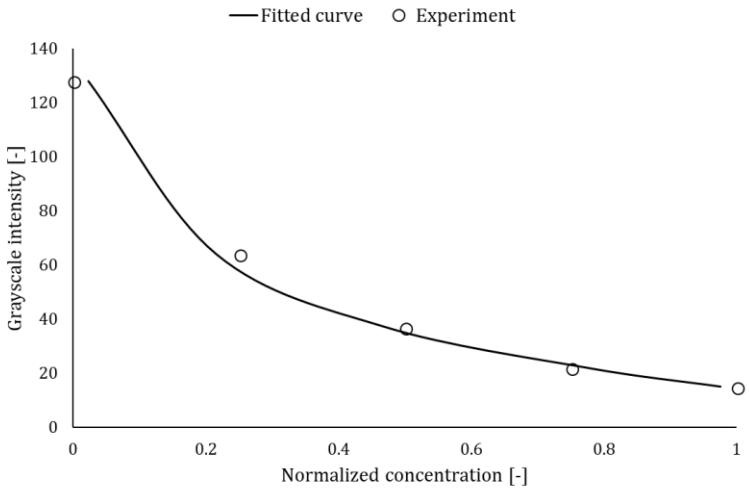

Table 2.3 Fitted parameters for relation grayscale value and normalized concentration
Figure 2.4 Relation between grayscale value and concentration for model 1. Points indicate experimental data, lines indicate fitted curve

2.3.3 Flow rate determination

Flow rates in porous media, on micro- and macroscale, vary enormously and depend on many

factors such as porosity, geology and water content. This provides a highly variable flow velocity field, varying as well as in space and in time. For determining a flow rate comparable to flow rates common in natural environments, microscale equations need to be taken into account. In this research, three different ink injection rates were used to obtain different Péclet numbers. The experiment was repeated with every model for three different flow rates: a low flow rate of 0.05 ml hr^{-1}, a medium flow rate of 0.1 ml hr^{-1}, and a high flow rate of 0.2 ml hr^{-1}, corresponding respectively to a flow velocity of approximately 3, 6 and 12 m day^{-1}. To ensure that hydrodynamic dispersion was the main transport mechanism, the Péclet number needed to exceed 1, indicating a greater advective transport rate compared to diffusive transport rate (eq. 3). Dispersion is caused by pore scale velocity fluctuations and it generates the spread of solutes, which at macroscopic scale is described using Fick's first law. Diffusion for particles dissolved in the liquid phase is slow and typical diffusion coefficients range between 10^{-10} and 10^{-9} m^2 s^{-1} (Hassanizadeh, 2016). Considering a characteristic length ranging between 0.437 - 0.477 mm (Table 2.1) and an assumed diffusion coefficient of 10^{-9} m^2 s^{-1}, the Péclet number exceeded the threshold of 1 extensively, as reported in Table 3.1. This showed that the influence of diffusion can be neglected in our experiments. Considering above estimates and calculations, a flow rate of 0.05 - 0.2 ml hr^{-1} is a realistic range to simulate naturally occurring flow velocities for single-phase flow.

Under unsaturated conditions, the same principles hold for the flowrate. However, two-phase flow is subject not only to viscous forces but also to capillary forces (Cense & Berg, 2009). The relative effect of viscous forces versus interfacial tension forces is calculated by the capillary number (Saffman & Taylor, 1958):

$$N_c = \frac{\mu v}{\sigma} \qquad (6)$$

with N_c as the capillary number [-], μ the fluid viscosity [$ML^{-1}T^{-1}$], v the average fluid velocity [LT^{-1}] and σ as the interfacial tension [MT^{-2}]. For residual and disconnected phases, the capillary number ranges from 10^{-5} to 10^{-7} for typical pressures, permeabilities and interfacial tensions, indicating capillary forces are greater than viscous forces. For connected phases, viscous forces are in equilibrium with capillary forces and the capillary number equals one. During displacement of one phase by the other, capillary numbers are greater than one, as viscous forces are larger than capillary forces (Cense & Berg, 2009). For this research, low capillary numbers in the range of 10^{-5} to 10^{-7} are preferred which correspond to a flow rate of 0.05 - 0.2 ml hr^{-1}. Therefore, one unsaturated experiment is carried out with a flow rate of 0.05 ml hr^{-1}.

2.3.4 Experimental procedure

After all air in the micromodel had been replaced by CO_2 gas, the model was saturated with water. The flow rate of the initial saturation was irrelevant, as long as the model became fully saturated and the flow rate was kept low enough in order not to damage the model. After the model was fully saturated, the ink solution was introduced in the model at a constant rate. Due to the wide inlet structure of the pore network, the ink has a fairly homogeneous front when entering into the pore network, which can be seen in Figure 3.1 of the Results section. The introduction of the ink solute continued until no change in ink concentration in the pore network was detected. As no change was identified, a few pulses of ink solution were injected in the model to ensure the model had a relatively uniform concentration of 100% ink solution. After this, the model was once more connected to a syringe pump containing water. Water was introduced then again at the same flow rate as the ink solution. The introduction of water continued until all ink in the model had left the pore network. This process was repeated for three different injection rates for all three models. In total, it resulted in 18 sets of experiments.

For the experiment under unsaturated conditions, micromodel 3 was first fully saturated with Fluorinert. Then, the Fluorinert-filled flow network is drained with water, at a low flowrate, in order to establish a certain water saturation. As soon as there was breakthrough of water at the outlet of the porous network and the residual saturation of the wetting phase did not change, a steady state was reached and the ink solution was introduced in the network. The flow rate of the ink solution for this experiment was 0.05 ml hr^{-1}. The injection of the ink solution continued until no change was detected. As no change was visible, the micromodel was connected to a syringe containing water and it was introduced in the porous network.

2.4 Data analysis

This chapter covers the data analysis of the experimental results. The images of the experiments were analysed in MATLAB (The MathWorks, Inc. (2018)) with an algorithm of a PhD student working at the Hydrogeology research group at Utrecht University (E.T. de Vries, personal communication, March 2018). This resulted in concentrations maps of ink and water dispersion in the pore network and accompanying breakthrough curves. Data of the breakthrough curves were inversely analysed with the CXTFIT program to obtain estimations of pore-water velocities and hydrodynamic dispersion coefficients.

2.4.1 Image alignment

During the experiments, movement of the micromodel and setup was inevitable. Even though the setup was placed on a vibration isolation table, the images showed a slight movement of a few micrometre between each frame. It was essential to align the images in order to obtain correct concentration fields and accompanying breakthrough curves. After many trials, it was concluded that aligning the images with a rigid registration plugin of ImageJ software works best so far (Preibisch et al, 2010; Rasband, 1997). Rigid registration transformed all images of each experiment into one coordinate system by translating and rotating all images consecutively to each other. It selected maxima in the images, analysed its neighbourhoods and matched all images according to these points. This procedure resulted in reasonably aligned images which were used for further processing.

2.4.2 Mask

To include only the pore space in the analysis, a mask was made of all three models for each experiment, resulting in total in nine masks. It covered all area except the pore space and was made of the first image of each experiment. The image was converted to a binary image and manually corrected for any errors in the pore network. The mask was then superimposed over all images, so only the pore space was read by the algorithm and all other areas were disregarded.

2.4.3 Filtering

As mentioned before, the micromodels were difficult to clean and it was almost impossible to get rid of all residue left on the micromodel. It was not uncommon that during the experiment dust particles and other fibres landed on the micromodel. Also, the setup and micromodel create small shadows around the grains, which are shown in Fig. 2.3 as the black outline around the grains. The shadows were in principal removed by the mask, but it could not be guaranteed that all shadows were covered. Therefore it was necessary to enhance the images such that these anomalies were deleted from the images. This was done by removing all bright and dark outliers,

using ImageJ software (Rasband, 1997). The difference between the images with and without outliers are shown in Appendix D.

2.4.4 Image analysis in MATLAB

The first step to analyse the images was to establish a relation between the concentration and grayscale value. In section 2.3.2 is explained how this was carried out. Each neighbourhood was assigned an average concentration value, and by using the relationship established between ink concentration and pixel intensity, the values were exponentially fitted. The full images were analysed and made into colour maps which correspond to concentrations, showing the dispersion of the ink solution. In able to obtain breakthrough curves, a plane perpendicular to the flow direction was chosen. It was essential that the chosen location was the same in all experiments and at the end of the porous network.

2.4.5 Breakthrough curves

The resulting breakthrough curves were plotted with relative concentration against pore volume. One pore volume was calculated as the total discharge over time divided by the cross sectional area of the porous network times the length and porosity, in other words the porous medium's volumetric capacity (Fetter et al., 2017):

$$PV = \frac{Discharge}{Capacity} = \frac{vt}{L} = \frac{Qt}{ALn} = t_r \qquad (7)$$

Where PV is the number of pore volumes [-], v the linear velocity [L/T], n is the porosity [-], A the cross sectional area [L^2], t is time [T], Q is total discharge [M^3T^{-1}] and L the length of the column [L]. The number of pore volumes was equal to a dimensionless time, t_r, also known as the hydraulic residence time (Fetter et al., 2017).

2.4.6 Advection-Dispersion model

The obtained breakthrough curves were fitted using the analytical model CXTFIT (Toride et al., 1995), which solved the advection-dispersion equation (eq. 1). The flow domain was three dimensional, however we assumed isotropic and homogeneous conditions in the porous medium which simplified the equation. The one dimensional ADE model simulated the average concentration of the plane perpendicular to the flow direction chosen in the images. The solute was not subject to adsorption as the ink solution is non-reactive. The initial and boundary conditions are shown in table 3.2.

Table 2.4 Initial and boundary conditions used in the CXTFIT model (Toride et al., 1995)

I.C. 1	$C(x,0) = C_i(x)$
I.C. 2	$Cf = C(x,t) - Pe^{-1}\frac{dC}{dx}$
B.C. 1	$\frac{dC(\infty,t)}{dx} = 0$
B.C. 2	$C = C(x,t) - Pe^{-1}\frac{dC}{dx}$

3 Results and Discussion

3.1 Analysis of experimental data

By processing the images of the experiments, nine breakthrough curves (BTCs) of ink injection in a micromodel saturated with water and nine BTCs of water injection in a micromodel initially saturated with ink solution were obtained. All images were made into coloured concentration maps, of which an example is given in Fig. 3.1. Concentration has been normalized during image processing. Figures 3.2, 3.3, and 3.4 show the BTCs for respectively model 1, 2, and 3 with varying flow rates. BTCs in figures 3.5, 3.6, and 3.7 show the results for different models with the same flow rates. Figures 3.2, 3.3, and 3.4 show the normalized concentration plotted against time, figures 3.5, 3.6, and 3.7 are plotted against pore volume. BTCs of all models with varying flow rates plotted against pore volume are shown in Appendix E. All BTCs of the water injection are shown in Appendix F. Fig. 3.1 shows the transport of the ink solution in model 2 at a flow rate of 0.2 ml hr^{-1}. The position of the breakthrough curve is outlined in black in the upper left image of Fig. 3.1.

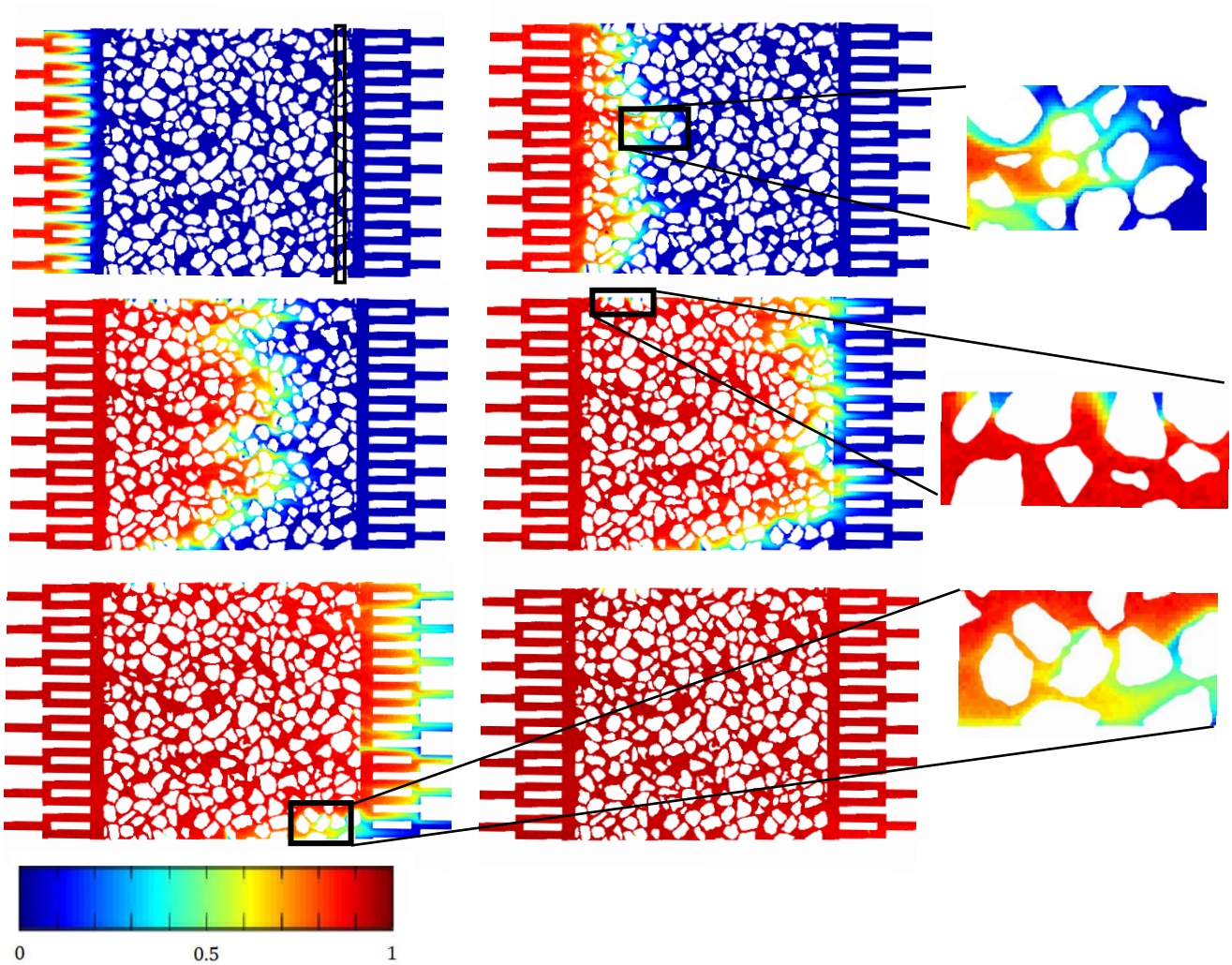

Figure 3.1 Concentration maps of ink injection in model 2 at flowrate 0.2 ml hr^{-1}. White-coloured areas correspond to solid areas. The areas where the ink solution is present in water are shown with a spectrum of colours between dark blue (zero concentration) and dark red (highest ink concentration). The position of the breakthrough curves is shown in the upper left image in white, positioned 10 mm after the solute enters the porous medium. On the right, zoomed- in images of pore space

Transport of the ink solution through the porous medium followed a similar pattern as shown as in Fig. 3.1 for all models and at all tested flow rates. Appendix G shows an example of the water injection for the same model at a flowrate of 0.2 ml hr^{-1}. Due to the structure of the inlet, the solute arrived at approximately the same time over the whole width of the porous medium which was essential for the assumption of 1D mesoscopic flow to obtain dispersivity based on the breakthrough curves. Preferential pathways can be clearly observed due to the heterogeneity of the pore network (Fig. 3.1 & App. G). These preferential pathways cause fingers of ink solution to form in the pore space as the ink solution is transported through the porous medium (Fig. 3.1). The preferential pathways were visible in each micromodel, regardless of the flow rate. The fingers were persistent through the experiment and finally merged just before reaching the end of the porous medium. Due to the complex pore structure and low velocity at the walls of the model, areas with low ink concentration were generated, resembling dead end pores (Fig. 3.1 & App. G). After a significant time, the ink concentration in these areas increased, mainly due to diffusion of the solute. The concentration of the front was relatively uniform and shows a high concentration gradient when spreading through the porous network. According to observations of the images of all experiments, the front seems to have kept the same concentration gradient when flowing through the porous network.

Table 3.1 shows the results from modelling the data of the saturated flow experiments with the CXTFIT model. The dispersion coefficient as well as the velocity represent averaged values for the flow domain at the particular location pointed out in Fig. 3.1. R^2 gives the coefficient of determination of the experimental data with the fitted data of the CXTFIT model.

Table 3.1 Data obtained from fitting experimental data with the CXTFIT model. Upper table showing data of ink injection in saturated porous network, lower table showing data of water injection in ink solution saturated porous network

Ink injection	**Flow rate [ml hr^{-1}]**	**v [mm s^{-1}]**	**D [mm^2 s^{-1}]**	**α_L [mm]**	**R^2**	**Pe [-]**
Model 1	0.05	0.040	0.0084	0.211	0.997	18.9
	0.10	0.079	0.0174	0.220	0.996	37.9
	0.20	0.148	0.0402	0.272	0.997	70.5
Model 2	0.05	0.039	0.0045	0.118	0.997	17.3
	0.10	0.072	0.0114	0.158	0.996	32.6
	0.20	0.142	0.0244	0.171	0.997	64.0
Model 3	0.05	0.035	0.0031	0.085	0.994	15.4
	0.10	0.069	0.0063	0.091	0.995	30.2
	0.20	0.136	0.0168	0.124	0.996	59.3

Water injection	**Flow rate [ml hr^{-1}]**	**v [mm s^{-1}]**	**D [mm^2 s^{-1}]**	**α_L [mm]**	**R^2**	**Pe [-]**
Model 1	0.05	0.032	0.0107	0.333	0.997	15.3
	0.10	0.063	0.0211	0.336	0.997	30.0
	0.20	0.128	0.0511	0.400	0.994	61.1
Model 2	0.05	0.032	0.0064	0.200	0.996	14.4
	0.10	0.063	0.0181	0.289	0.995	28.2
	0.20	0.126	0.0378	0.301	0.994	56.5
Model 3	0.05	0.023	0.0041	0.180	0.997	10.1
	0.10	0.060	0.0105	0.174	0.995	26.3
	0.20	0.105	0.0282	0.269	0.995	45.8

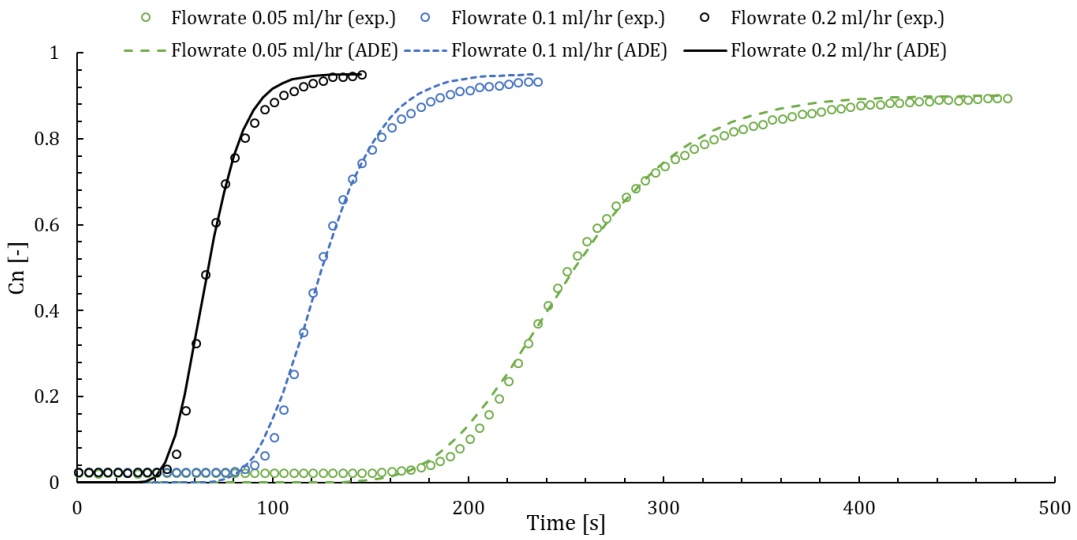

Figure 3.2 BTCs of model 1 for three different flowrates (0.05, 0.1, and 0.2 ml hr^{-1}). Points indicate experimental data, lines indicate fit by ADE-model in CXTFIT

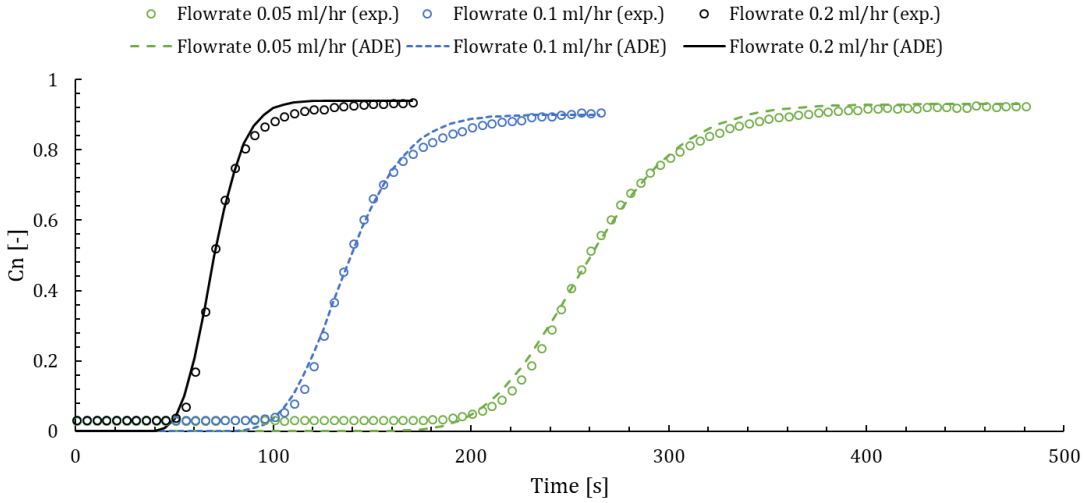

Figure 3.3 BTCs of model 2 for three different flowrates (0.05, 0.1, and 0.2 ml hr^{-1}). Points indicate experimental data, lines indicate fit by ADE-model in CXTFIT

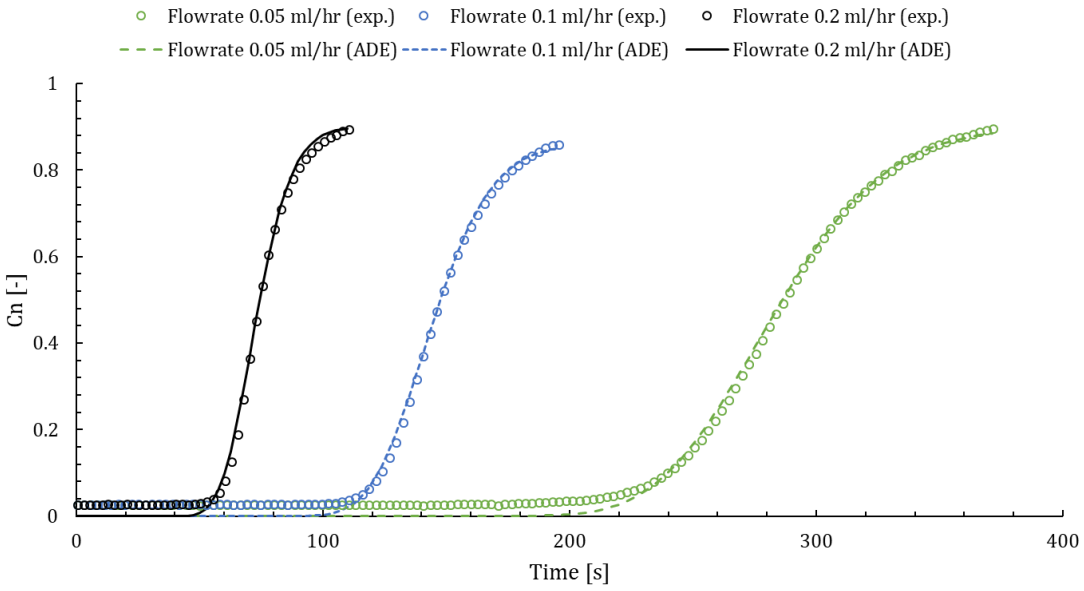

Figure 3.4 BTCs of model 3 for three different flowrates (0.05, 0.1, and 0.2 ml hr^{-1}). Points indicate experimental data, lines indicate fit by ADE-model in CXTFIT

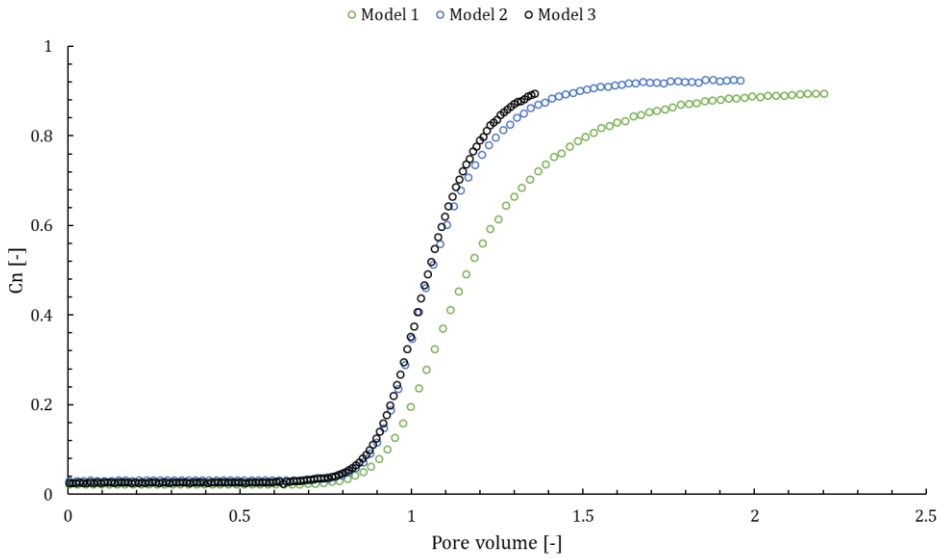

Figure 3.5 BTCs of models 1, 2, and 3 at flowrate 0.05 ml hr^{-1}

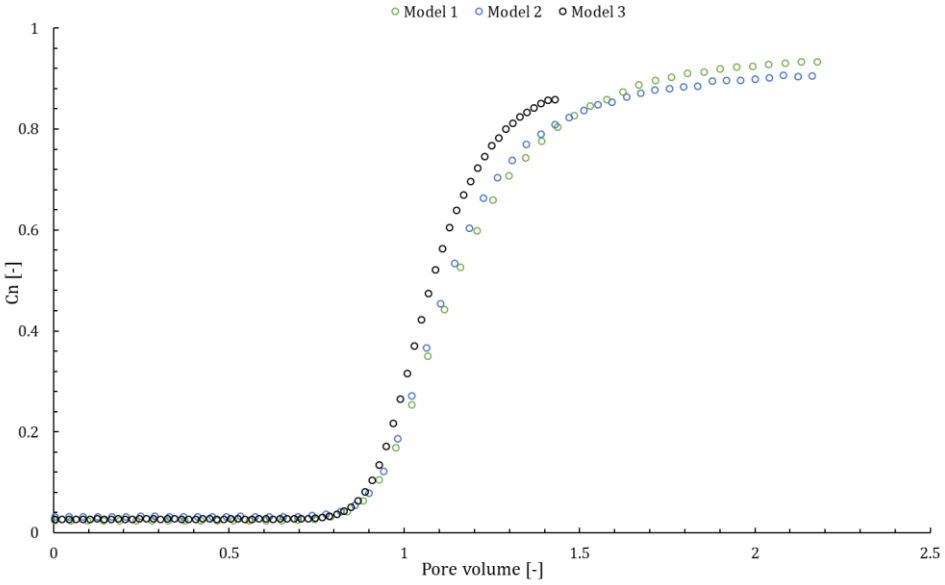

Figure 3.6 BTCs of models 1, 2, and 3 at flowrate 0.1 ml hr^{-1}

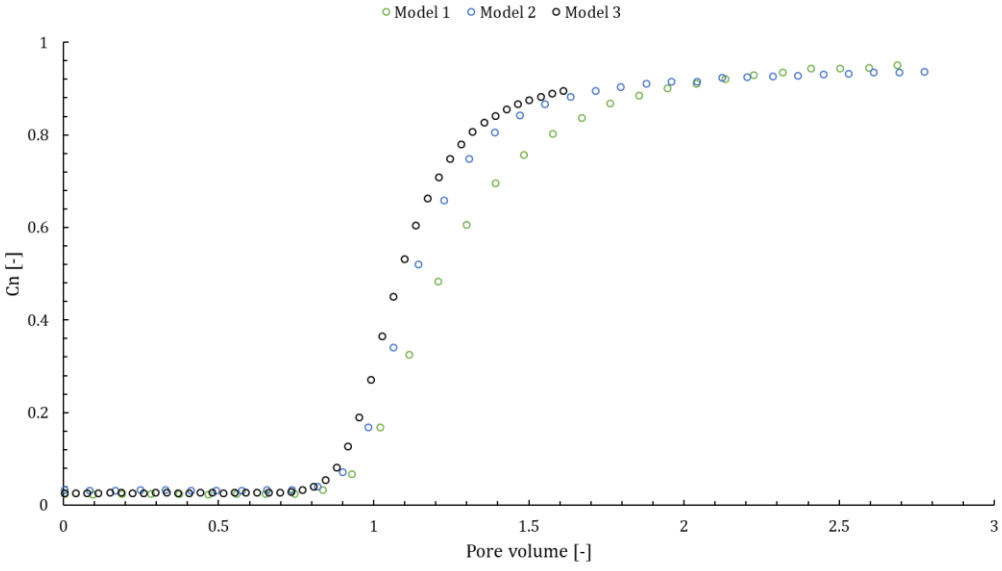

Figure 3.7 BTCs of models 1, 2, and 3 at flowrate 0.2 ml hr^{-1}

Table 3.1 also shows the Péclet number, calculated according to eq. 4 with an assumed diffusion coefficient of 10^{-9} m^2 s^{-1}. Note that if the assumption of the diffusion rate would have been 10^{-10} m^2 s^{-1}, the Péclet number would be increased by tenfold. Therefore it is likely to assume that the high concentration gradient is due to a high Péclet number (Pe >> 1). It shows that for the lowest flow rate of 0.05 ml hr^{-1}, the Péclet number largely exceeds 1 and increases with an increasing flow rate and a decreasing porosity. It can be assumed that the concentration front differs between the different flow rates, due to increased diffusion with lower flow rates. The agreement between the fitted values of the ADE model and the measured values of all experiments is reasonably good (>0.994), as outlined in table 3.1. According to the BTCs, the concentration values of the experiments do not start exactly at a concentration value of 0. This is likely as a results of noise in the images due to the residue left on the micromodels and the small spread in pixel intensity level assigned to each concentration value. During image processing, the pixels with a negative value are set to zero, which also contributes to noise in the concentration maps. The BTCs do not reach a concentration value of 1 for the injection of the ink solution. A possible cause for this is dispersion of the solution. For the ink concentration to reach a normalized value of one, the experiment would have had to be continued for a much longer time. The BTCs of the water injection start at a normalized ink concentration of 1 (App. F), due to extra concentration pulses given during the experiment to assure that there was a reasonable uniform concentration of ink solution in the porous medium before starting the introduction of water.

3.1.1 Analysis of flow rate dependency

When comparing the BTCs of each model (Fig. 3.2, 3.3, 3.4 & App. F), it is interesting to see as the flowrate is doubled, breakthrough of the injected fluid takes almost exactly twice as long. It shows that with a doubling flow rate, the average velocity also increases by twofold. This was also corroborated by the analytical analysis and shown in table 3.1. Regarding eq. 3, the dispersivity values found (table 3.1) are of the same magnitude as expected. The breakthrough curves of all models show a similar trend with increasing flow rate; the slope of the breakthrough curves becomes steeper with an increase in flow rate, which holds for all models. Approximately one pore volume is needed to reach breakthrough for all models, regardless of the flow rate (App. E & F), and is shown in fig. 3.10. Outlined in table 3.1 are the dispersivity values, which show the same trend which can be observed from the breakthrough curves. The dispersivity values obtained by the ADE model show an increase in dispersivity as the flow rate increases. Interesting to see is that the dispersion coefficient, and therefore also dispersivity, is larger for the injection of water compared to the injection of ink, despite being injected under similar conditions.

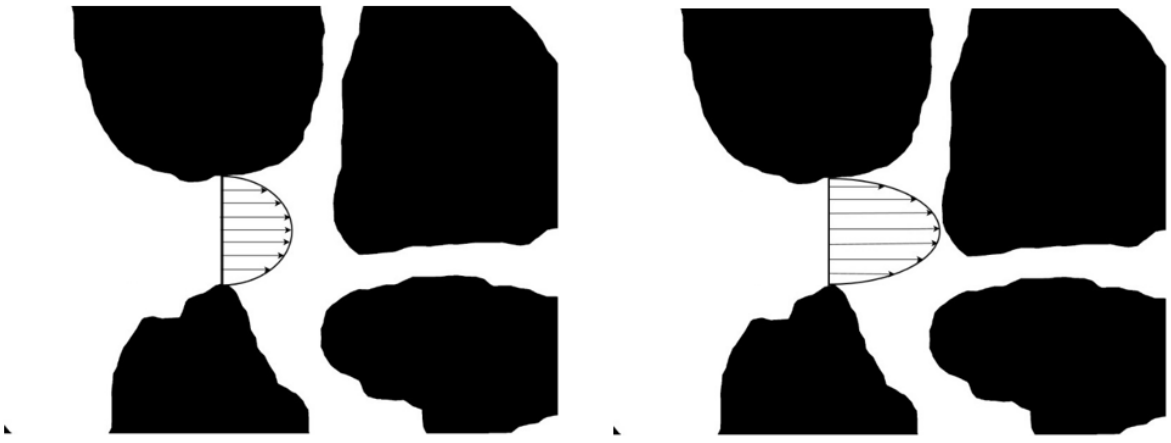

Figure 3.8 Flow velocity distribution between grains, with on the left-hand side a lower flow velocity and on the right a higher flow velocity

Key to understanding dispersion of non-reactive solutes in porous media is the velocity changes in combination with the velocity distribution of the particles along the particles trajectory. As the flow rate decreases, the variability of ink particle velocities decreases as well. This results in a decrease in velocity gradient which an example is shown in Fig. 3.8. A lower variability of ink particle velocities leads to less mixing of the ink solution in the pore space, which in turn generates less dispersion and a lower value for dispersivity. Fig. 3.9 shows flow rate plotted versus dispersivity for the three micromodels. Micromodel 1 and 3 have almost precisely the same dispersivity for flowrate 0.05 and 0.1 ml hr^{-1}, however it increases with a flow rate of 0.2 ml hr^{-1}. The increase in dispersivity for micromodel 2 shows a different trend compared to the other micromodels; a doubling in flowrate from 0.05 to 0.1 ml hr^{-1} shows a bigger increase in dispersivity compared to micromodel 1 and 3. However, from 0.1 to 0.2 ml hr^{-1}, dispersivity increases less than compared to micromodel 1 and 3. This trend can be observed for both the ink injection and water injection. It is a possibility that the observed trend is a result of the inaccuracy of the fit of the grayscale intensity values to concentration levels in the images. The observed trend could also be due to the heterogeneity of the porous medium; if the BTCs were measured at a different position, it might give a different result. To rule this out, the BTCs should be measured at various locations in the porous medium.

It is clear that the dispersivity increases with an increasing flow rate in a non-linear way. Previous researches show the existence of a linear relationship between the longitudinal dispersivity coefficient and flow rate at relatively high rates of flow (Bear, 1979; Gerritse & Singh, 1988). At lower flow rates, the relationship becomes nonlinear due to an increase in molecular diffusion. A similar trend can be observed for our results. It is a possibility that the flow rates are relatively small compared to the scale of the porous medium and molecular diffusion has a bigger influence than previously assumed. This is also backed when looking at Péclet numbers of the experiments and the accompanying regime of dispersion. According to Pfannkuch (1963), there are five regimes in which dispersion can be delimited, of which the Péclet numbers resulting of this research are categorized in the 'interference' regime ($5<Pe<400$ to 10^3). Dispersion dominates in this regime, however diffusion cannot be neglected due to transverse molecular diffusion interfering with longitudinal convection which tends to decrease dispersion (Rose, 1973; Pfannkuch, 1963). With both the assumed diffusion coefficient of 10^{-9} m^2 s^{-1} or using the 10^{-10} m^2 s^{-1}, the Péclet number would still be categorized in the 'interference' regime.

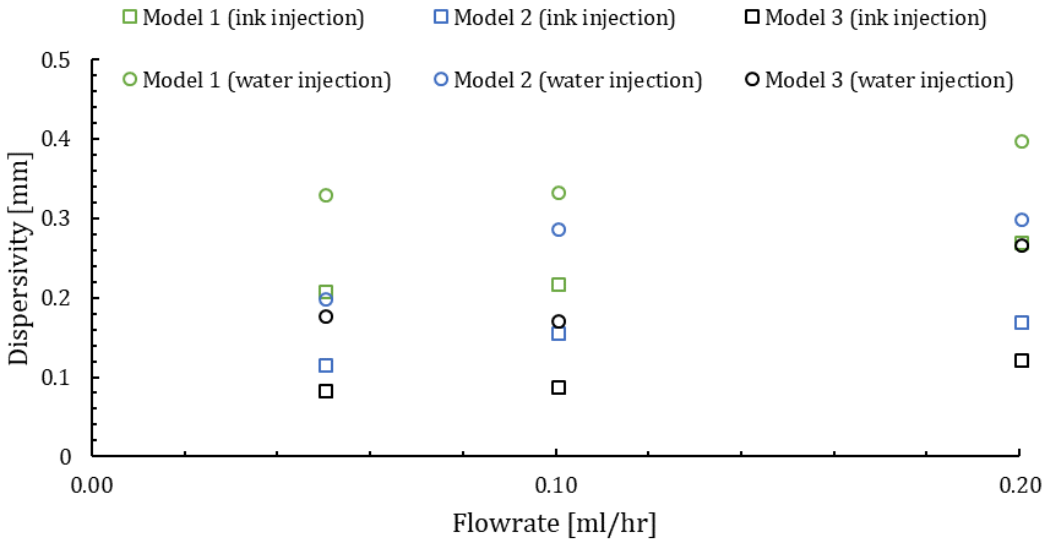

Figure 3.9 Dispersivity plotted against flow rate for all micromodels

Bijeljic et al. (2004) also show that with a Péclet number between 1 and 100, dispersion has a pronounced influence on the mixing of a solute. Therefore, it can be said that dispersion is the main mechanism causing mixing of the ink solution in the porous medium as previously assumed. The results clearly show that dispersivity does significantly increases with an increase in the flow rate. The relation between dispersivity and flow rate identified in this study is in accordance with previous research (e.g. Hiby, 1962; Rose, 1973).

3.1.2 Analysis of porosity dependency

Figures 3.5, 3.6, 3.7 and Appendix F show the BTCs of the micromodels compared to each other, plotted as pore volume. Due to a time correction for micromodel 3, the breakthrough curves were not continued for more pore volume compared to micromodel 1 and 2.

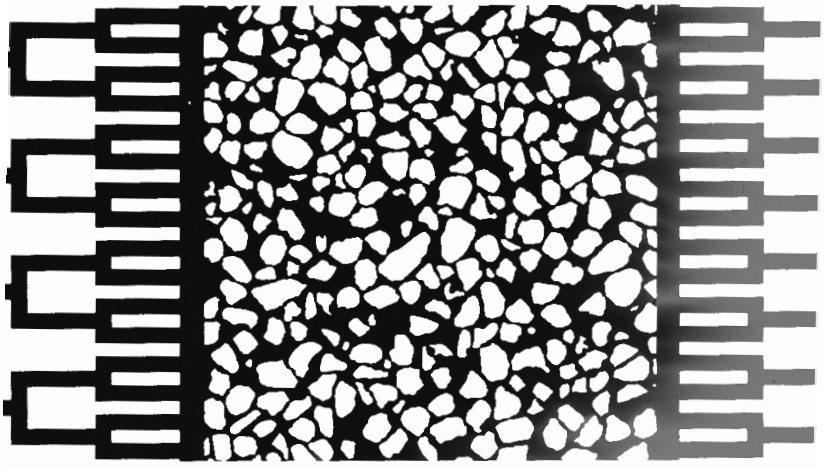

Figure 3.10 Image of ink injection in micromodel 2 at flow rate 0.05 ml hr^{-1}, at mean breakthrough. White-coloured areas correspond to solid areas. The areas where the ink solution is present in water are shown with a spectrum of colours between light grey (zero concentration) and dark grey (highest ink concentration)

Fig. 3.10 shows the image of micromodel 2 at breakthrough; the images of the other micromodels at breakthrough are very similar as the one shown in Fig. 3.10. Fig. 3.5 to 3.7 and Appendix F show a small variation between the models for the pore volume required to reach breakthrough. The variation between the models however is very small, so the differences can be neglected. The breakthrough curves of micromodel 3 show the steepest slopes, which becomes gradually less steep with a decreasing porosity. This is in correspondence with the data from table 3.1, which shows a similar trend. The dispersivity values obtained by the ADE model show an increase in dispersivity as the porosity decreases.

Due to the increased pore space of micromodel 2 and 3, the volume in which the ink solution can disperse is significantly larger compared to micromodel 1. The increase in pore volume leads to a smaller variability of particle velocity, which results in less dispersion of the ink solution in the porous medium. This mechanism is similar as the one discussed above in the previous section. Amiri & Vafai (1993) also state that the velocity profile in porous media is sensitive to any variation in porosity, which corroborates with our findings. It is a possibility that the tortuosity of the medium decreases with an increasing porosity. This could lead to less mixing of the ink solution as the pathway of the particles would become shorter, and therefore less dispersion would take place. This in turn could lead to lower dispersivity values. However a clear relation between tortuosity and porosity has not been established yet (Shen & Chen, 2007; Matyka et al., 2008). Fig. 3.11 shows dispersivity plotted against porosity. Again, a linear increase in porosity shows a non-linear decrease in dispersivity.

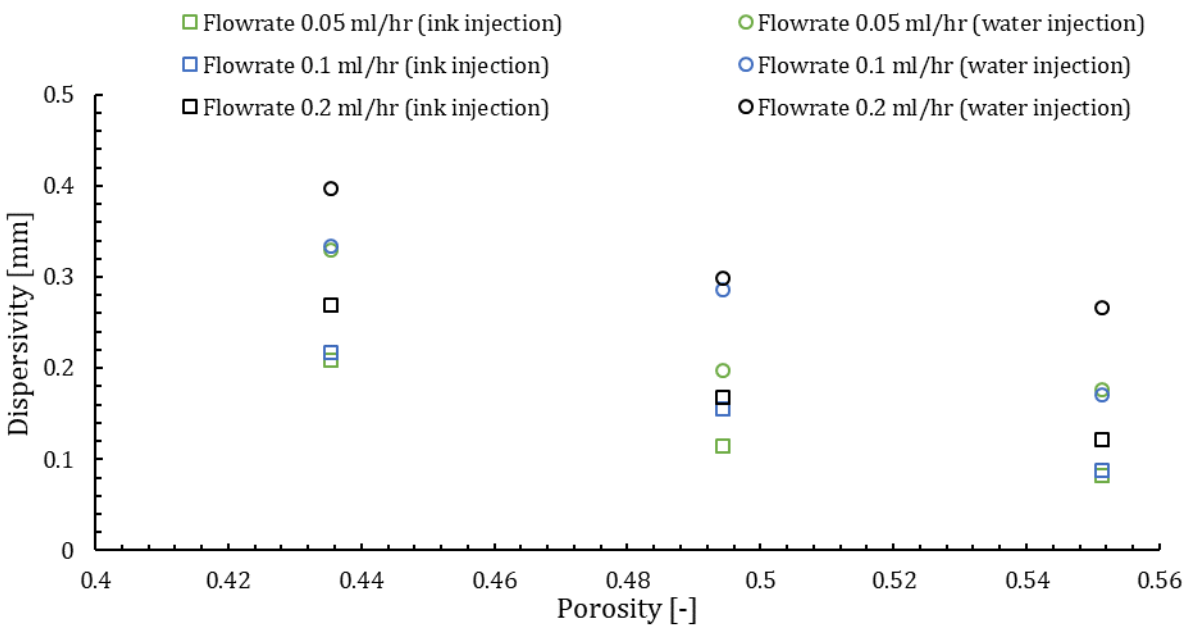

Figure 3.11 Dispersivity plotted against porosity

Previous research has shown that dispersion is not only a function of porosity, but also greatly depends on pore radius distribution, pore coordination and blockage, and the orientation of pores with mean flow direction (Sahimi et al, 1986). These elements are also changed with an alteration in porosity, and can be a possible cause of the non-linearity found in the relation between porosity and dispersivity. Research carried out by Edwards et al. (1991) with circular cylinder models with different packing arrangements also show that dispersivity decreases with increasing porosity, corroborating with our findings. It is clear that the change in porosity, in homogeneous and heterogeneous models, relates to change in dispersivity, however the exact relation has not been established thus far.

3.2 Unsaturated experiment

Fig. 3.12 shows real-time images taken of the two-phase flow experiment. After the model was saturated with Fluorinert, water was introduced at a flow rate of 0.05 ml hr^{-1}. The images show that the inlet of the model was only partially saturated with water, with Fluorinert blocking the other part of the inlet structure. With this particular inlet structure, it would be difficult to displace all Fluorinert from the inlet. There is a strong possibility that, even with a lower flow rate, Fluorinert would still be trapped in the corners. Residual saturation of Fluorinert was established as breakthrough took place. As soon as steady state was reached, the ink solution was introduced and transported through the water-filled areas. After no change in ink concentration was noticed, water was introduced again, in order to flush the non-wetting phase filled area. As shown in Fig. 3.12 (bottom right), many dead end pores were created due to a low flow velocity, making diffusion likely the key transport mechanism to transport the ink concentration through the porous medium after water was injected. It is clear that the models are useful for two phase flow experiments, which has also been proven by previous research (e.g. Karadimitriou et al., 2016; Jiménez-Martínez et al., 2015) for both heterogeneous as homogeneous porous networks. However, it would be advised to change the inlet structure to prevent Fluorinert of blocking the inlet and to have a homogeneous front entering the porous network.

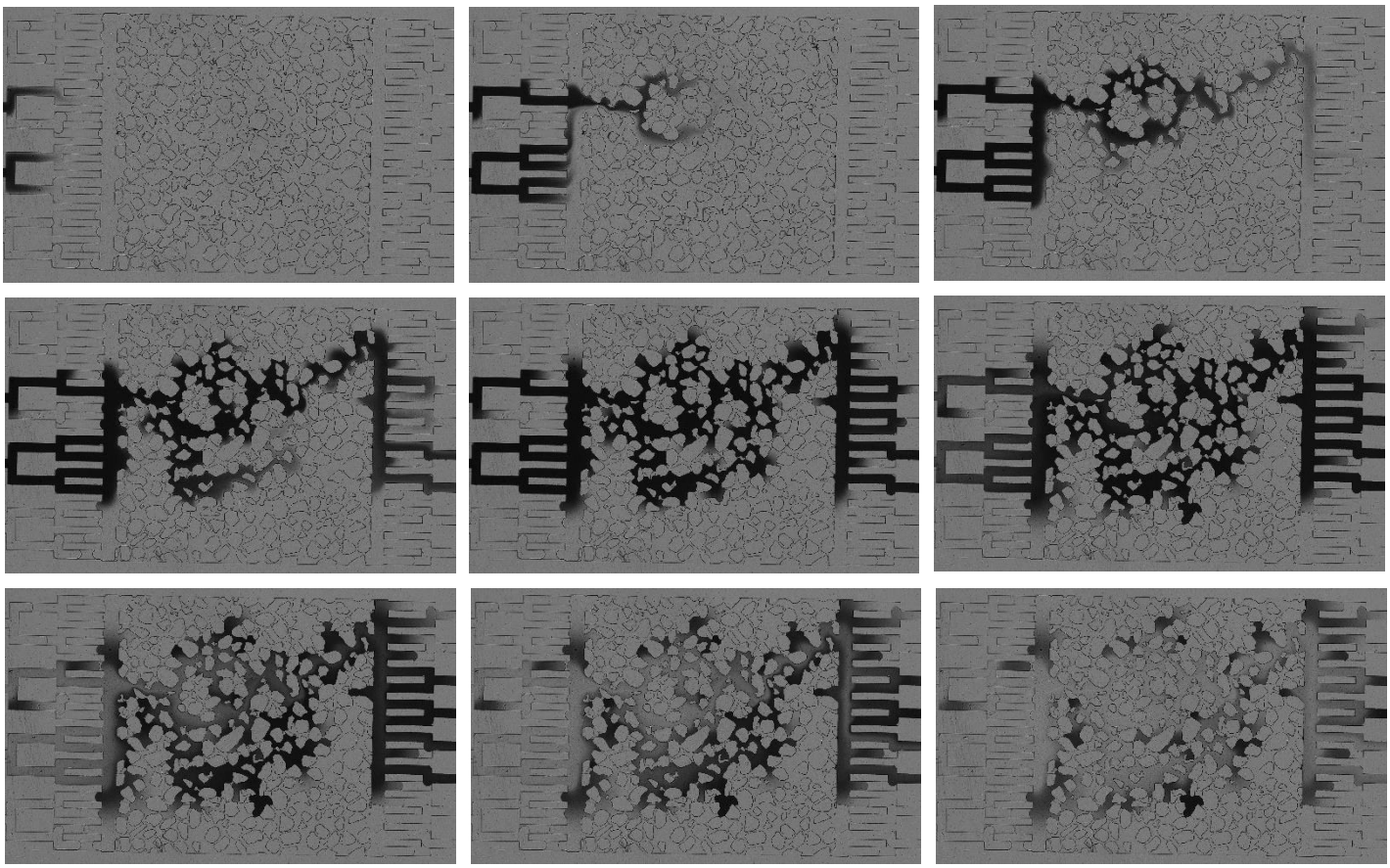

Figure 3.12 Images of the two-phase flow experiment with model 2 with flowrate 0.05 ml hr^{-1}. Top left the start of the experiment, bottom right the end result. The areas where ink concentration was present are shown in a spectrum of grey between light grey (low ink concentration) and dark grey (high concentration)

4 Conclusion

We researched flow rate and porosity dependency of solute dispersivity on pore scale level. Three PDMS micromodels were developed with varying porosity (n = 0.435, 0.494, and 0.551) but similar pore structure and connectivity. Single-phase flow experiments were carried out under similar conditions but with varying flow rates (Q = 0.05, 0.1, and 0.2 ml hr^{-1}). An ink solution was injected in the micromodels saturated with water at these flowrates, and water was injected in the models saturated with the ink solution. Real-time images of the experiments were recorded, resulting in a set of in total 18 BTCs. The resulting BTCs were fitted using an algorithm in order to relate grayscale intensity values of the images to solute concentration levels in the porous network. Obtaining correct concentration values from the images is a difficult procedure, which requires experimental precision and high quality images. To obtain transport parameters, the BTCs were fitted using analytical solutions of the ADE by applying the CXTFIT model. The resulting parameters showed that increased porosity results in decreasing dispersion and therefore also decreasing longitudinal dispersivity. An increase in flow rate was found to increase mixing of the solute in the saturated micromodel, and thus also increasing the longitudinal dispersivity. Both flow rate as the porosity dependency of solute dispersivity showed a non-linear trend. Previous research has shown that a non-linear relation can be explained by increased diffusion at low flow rates. However, it is a possibility that the non-linearity is generated by inaccuracies of the fit between the images and concentration levels.

We have showed with this research that similar experiments can be performed under two-phase conditions with this heterogeneous pore structure and visualization setup. However, the current inlet structure prevents the fluid of easily infiltrating the micromodel with a uniform concentration front. A change in inlet structure would make it easier to create a uniform concentration front for future unsaturated experiments.

Future research

In this study, we used single-phase conditions to study flow rate and porosity dependency of solute dispersivity. Further research can be done to the influence of flow rate and porosity on solute dispersion under unsaturated conditions. New techniques have been developed in order to make PDMS hydrophilic, creating the possibility of carrying out experiments with water as the wetting phase and making two-phase flow experiments easier to carry out.

Another method to research the influence of porosity on dispersivity can be done by changing the porous network. A similar level of porosity but different grain distribution can prove more insight in the relation between porosity and solute dispersion. Also changing the network from a heterogeneous to a homogeneous network with circular pillar structure can be used to research the effect of heterogeneity on solute dispersion.

A Layout micromodels

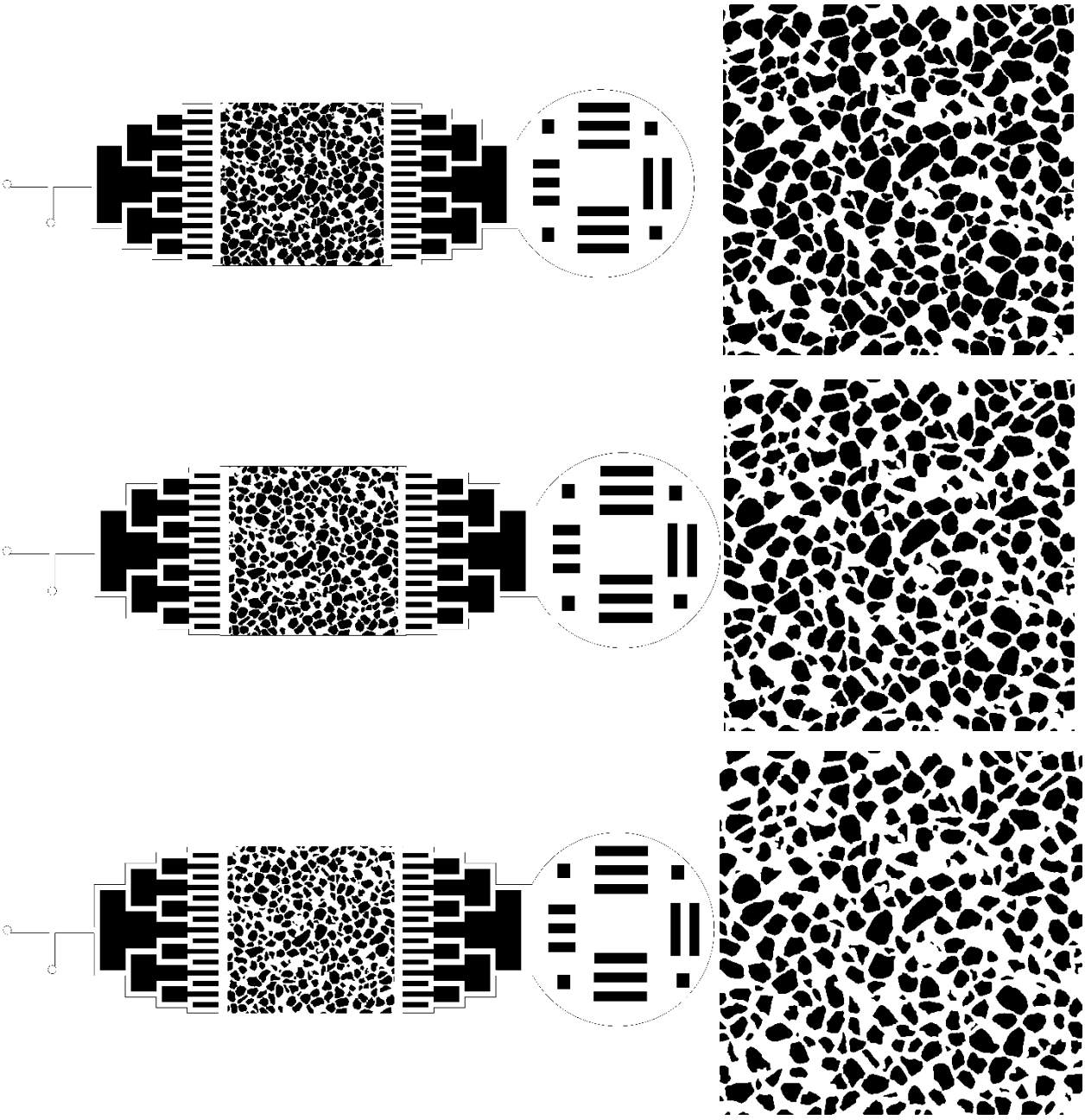

Figure A.1 From top to bottom micromodel 1, 2 and 3. On the left the full model including outlet (left side of image) and two inlets (right side of image)

B Concentration effect on pixel intensity

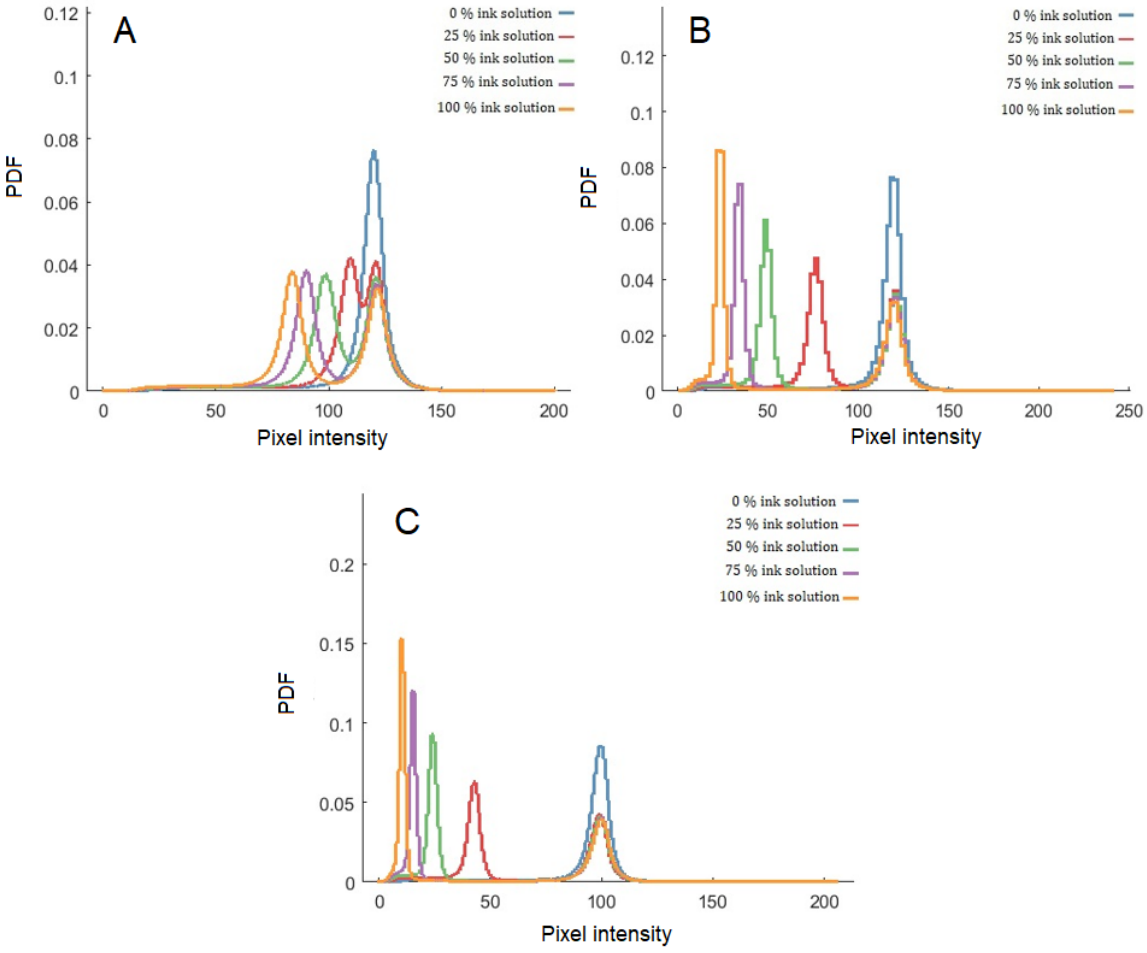

Figure B.1 Figure shows the effect of injecting ink solution concentration. In a clockwise direction, the histograms of a low ink concentration of 10 % ink & 90 % water (A), a medium ink concentration of 50 % ink & 50 % water (B), and a high ink concentration of 75 % ink & 25 % water (C) are shown, with on the y-axis probability density function and on the x-axis the pixel intensity value. Above experiments have been carried out under similar illumination and camera conditions. NOTE: the axis of the histograms differ

Figure B.1 shows the effect of the ink concentration used in the experiments. As mentioned before, the Beer-Lambert law states that the relation between concentration and pixel intensity is exponential. As shown in figure A.1, it is clear that the a solution with a low ink concentration (upper left) does not show this relation. However, the solution with a high ink concentration does show this relation; the intensity of the pixel value decreases exponentially with the concentration of the ink. The second peaks shown above are due to the fact that no mask was used while generating the histograms. Therefore the histograms show the pixel intensity of the grains, which during the experiments were disregarded by the use of a mask.

C Calibration data

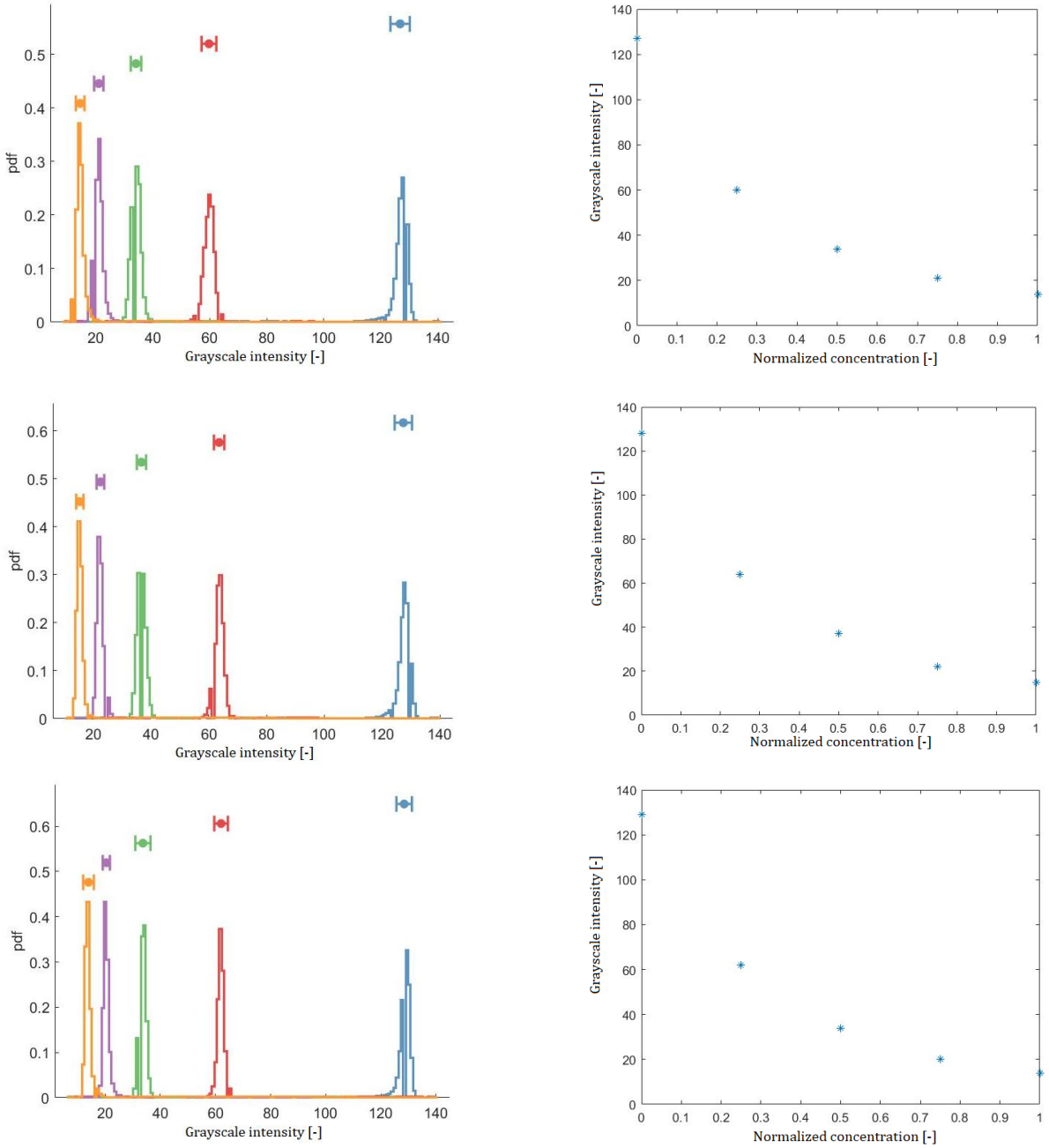

Figure C.1 Histograms and median values for five known ink solutions for micromodel 1 (top), micromodel 2 (middle), and micromodel 3 (bottom). Both images show an exponential decrease with an increase in ink concentration. The accompanying exponential function and parameters can be found in section 2.3.2

D Difference BTC outliers

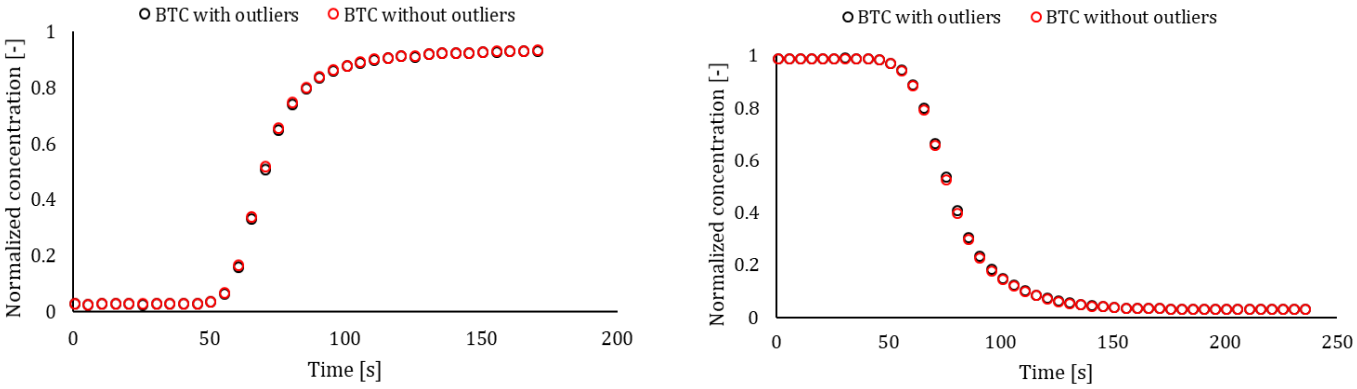

Figure D.1 Ink injection (left) and water injection (right) for model 2 at flowrate 0.05 ml hr^{-1}. Black points indicate analysed images with outliers, red points indicate analysed images without outliers

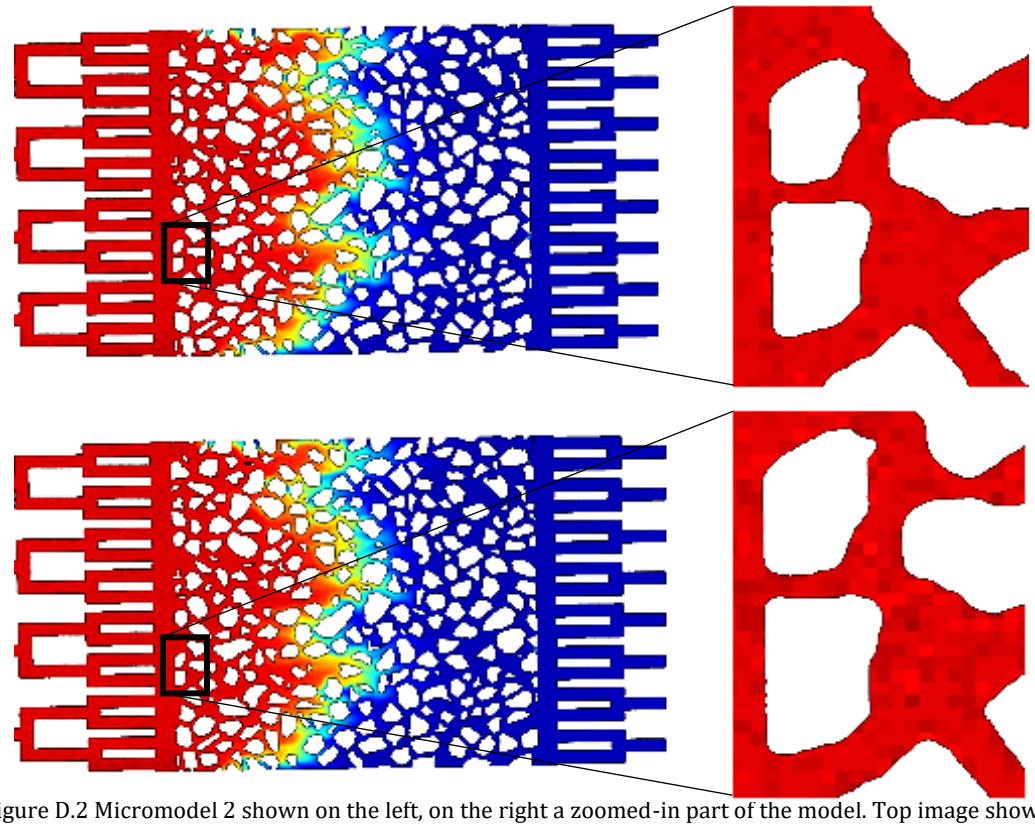

Figure D.2 Micromodel 2 shown on the left, on the right a zoomed-in part of the model. Top image shows concentration map without outliers, bottom image shows concentration map with outliers

As shown as in figure D.1, there is almost no difference in breakthrough curve between the images with outliers and the ones without. Figure D.2 shows a random image of micromodel 2 during one of the experiments. The noise in the top image is significantly less than in the bottom image, due to the removal of dark and bright outliers in the images.

E BTCs of ink injection

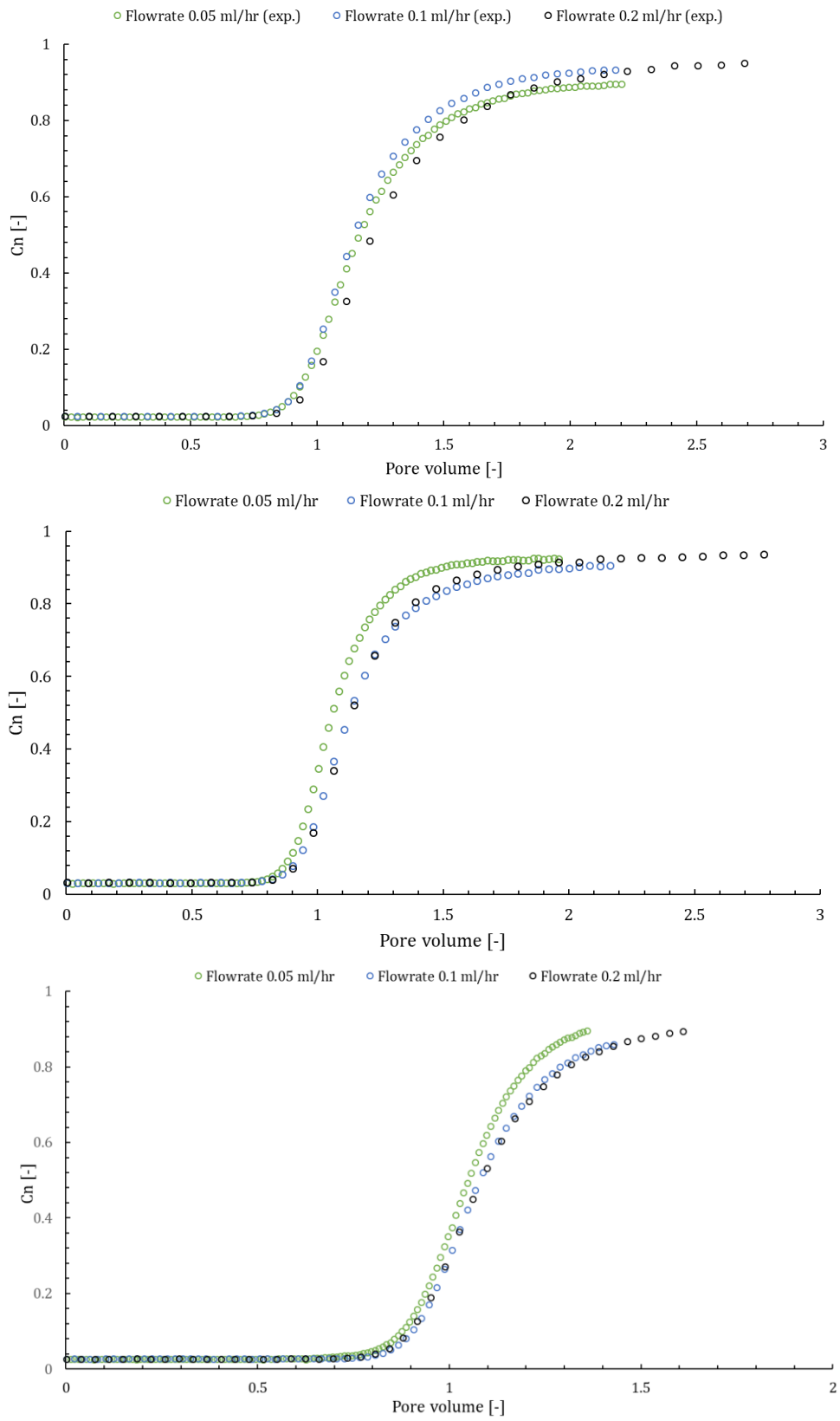

Figure E.1 Breakthrough curves of ink injection of model 1 (top), 2 (middle), and 3 (bottom), with normalized concentration plotted against pore volume

F BTCs of water injection

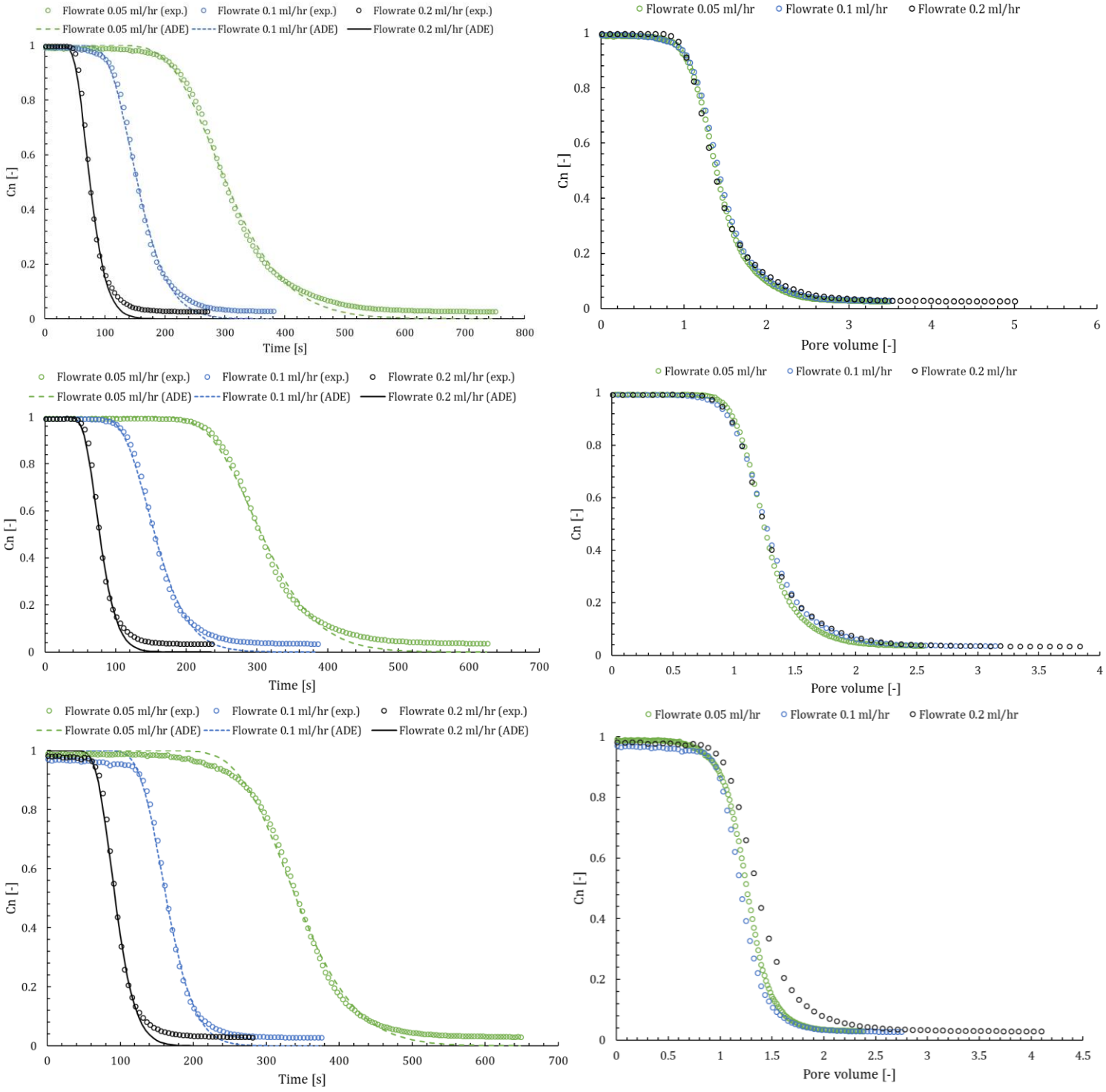

Figure F.1 Breakthrough curves of water injection of model 1 (top), model 2 (middle), and model 3 (bottom). On the left normalized concentration plotted against time, on the right plotted against pore volume

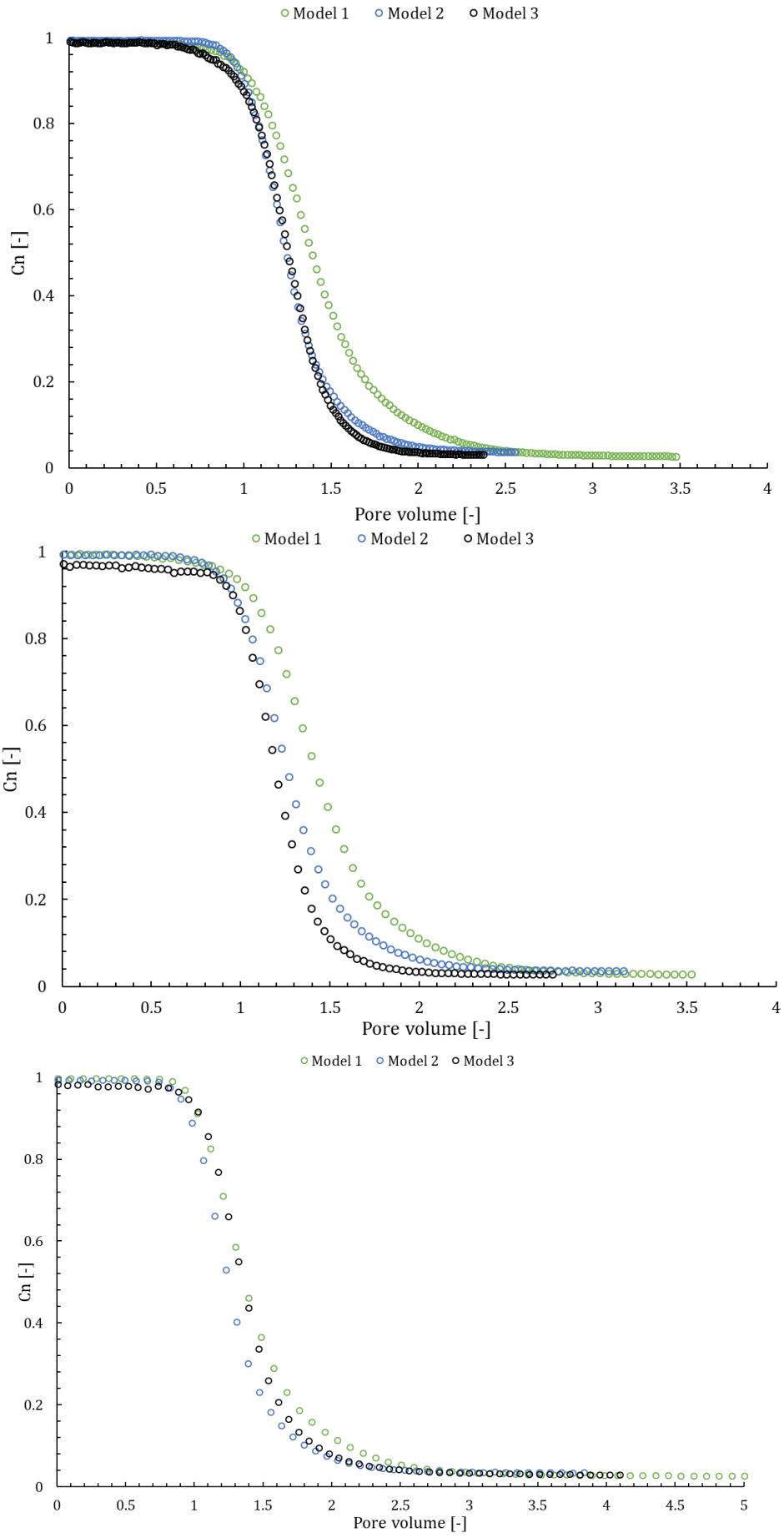

Figure F.2 Breakthrough curves of water injection of flowrate 0.05 ml hr^{-1} (top), 0.1 ml hr^{-1} (middle), and 0.2 ml hr^{-1} (bottom), with normalized concentration plotted against pore volume

G Concentration maps water injection

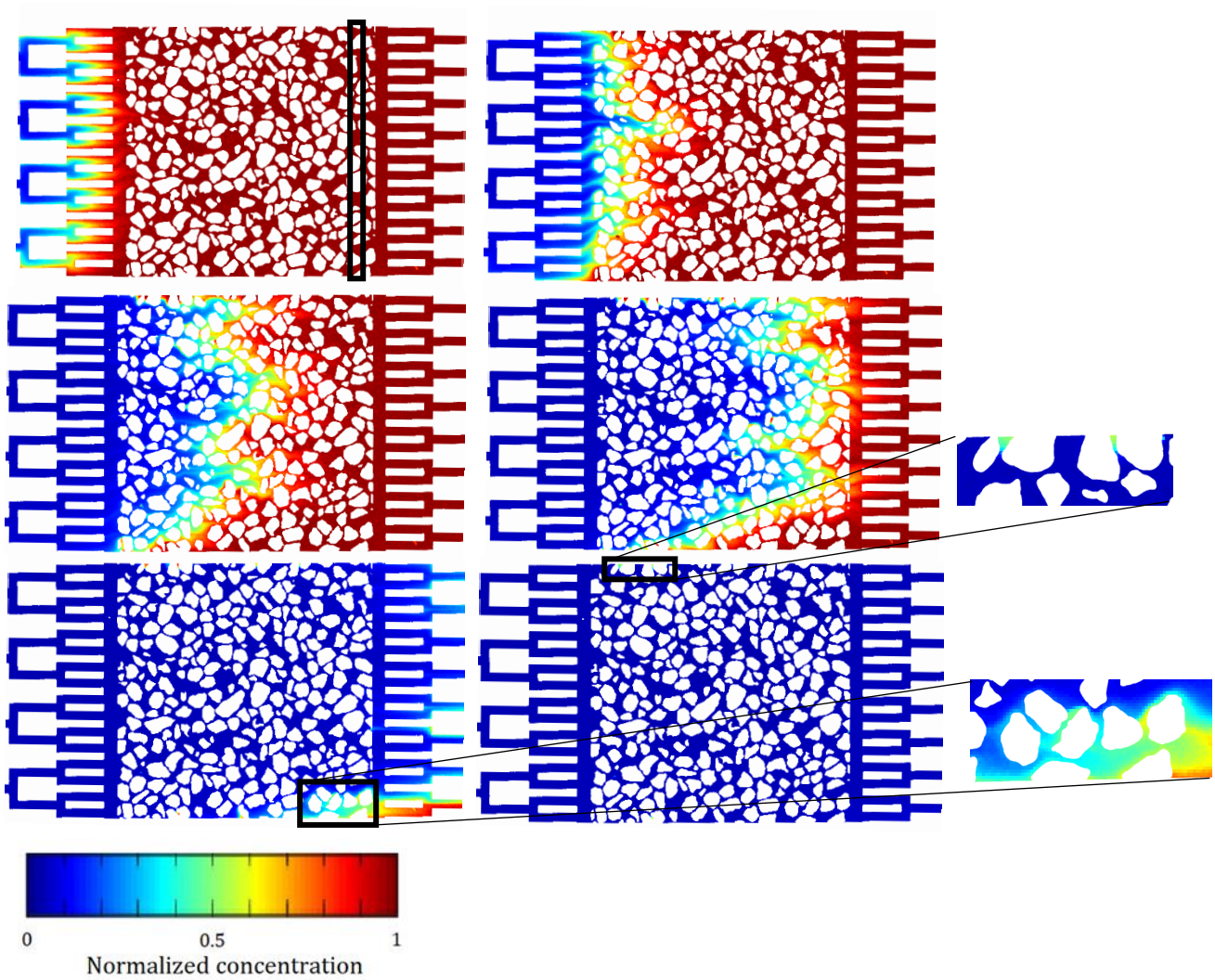

Figure G.1 Concentration maps of water injection in model 2 at flowrate 0.2 ml hr^{-1}. White-coloured areas correspond to solid areas. The areas where the ink solution is present in water are shown with a spectrum of colours between dark blue (zero concentration) and dark red (highest ink concentration). The position of the breakthrough curves is shown in the upper left image in black, positioned 10 mm after the solute enters the porous medium. On the right, zoomed-in images of pore space with higher ink concentration

References

3M. (2000). *Fluorinert Electronic Liquid FC-43 Product Information* [PDF File]. Retrieved from https://multimedia.3m.com/mws/media/648890/fluorinert-electronic-liquid-fc-43.pdf

Amiri, A., & Vafai, K. (1994). Analysis of dispersion effects and non-thermal equilibrium, non-Darcian, variable porosity incompressible flow through porous media. *International Journal of Heat and Mass Transfer*, *37*(6), 939-954.

Bear, J. (1979). Hydraulics of Groundwater. McGraw-Hill, New York, N.Y., 225-239.

Bear, J. (1988), *Dynamics of Fluids in Porous Media*, Dover, New York.

Bear, J., & Cheng, A. H. D. (2010). *Modeling groundwater flow and contaminant transport* (Vol. 23). Springer Science & Business Media.

Bijeljic, B., Muggeridge, A. H., & Blunt, M. J. (2004). Pore-scale modeling of longitudinal dispersion. *Water Resources Research*, *40*(11).

Caplin, J. D., Granados, N. G., James, M. R., Montazami, R., & Hashemi, N. (2015). Microfluidic Organ-on-a-Chip Technology for Advancement of Drug Development and Toxicology. *Advanced healthcare materials*, *4*(10), 1426-1450.

Chatenever, A., & Calhoun, J. C. (1952, June 1). Visual Examinations of Fluid Behavior in Porous Media - Part I. *Society of Petroleum Engineers*. doi:10.2118/135-G

Cense, A. W., & Berg, S. (2009, September). The viscous-capillary paradox in 2-phase flow in porous media. In *International Symposium of the Society of Core Analysts held in Noordwijk, The Netherlands* (pp. 27-30).

Corapcioglu, Y. M., Chowdhury, S., & Roosevelt, S. E. (1997). Micromodel visualization and quantification of solute transport in porous media. *Water resources research*, *33*(11), 2547-2558.

Corapcioglu, M. Y., & Fedirchuk, P. (1999). Glass bead micromodel study of solute transport. *Journal of contaminant hydrology*, *36*(3), 209-230.

Dahan, O. (2016, April). Vadose Zone Monitoring as a Key to Groundwater Protection from Pollution Hazard. In *EGU General Assembly Conference Abstracts* (Vol. 18, p. 4095).

Fetter, C. W., Boving, T., & Kreamer, D. (2017). *Contaminant hydrogeology*. Waveland Press.

Fitts, C.R. (2012) *Groundwater Science* Academic Press.

Freeze, R. and Cherry, J. (1979). Groundwater. Prentice-Hall, Englewood Cliffs, N.J.

Gerritse, R. G., & Singh, R. (1988). The relationship between pore water velocity and longitudinal dispersivity of Cl−, Br−, and D2O in soils. *Journal of hydrology*, *104*(1-4), 173-180.

Hassanizadeh, S.M. (2016). Hydrogeological Transport Phenomena [Lecture notes]. Retrieved from www.uu.blackboard.com

Hiby, J. W. (1962). Longitudinal and transverse mixing during single-phase flow through granular beds. *Interaction between Fluids & Particles*, 312-325.

Huh, D., Matthews, B. D., Mammoto, A., Montoya-Zavala, M., Hsin, H. Y., & Ingber, D. E. (2010). Reconstituting organ-level lung functions on a chip. *Science*, *328*(5986), 1662-1668.

Jiménez-Martínez, J., Anna, P. D., Tabuteau, H., Turuban, R., Borgne, T. L., & Méheust, Y. (2015). Pore-scale mechanisms for the enhancement of mixing in unsaturated porous media and implications for chemical reactions. *Geophysical Research Letters*, *42*(13), 5316-5324.

Jiménez-Martínez, J., Le Borgne, T., Tabuteau, H., & Méheust, Y. (2017). Impact of saturation on dispersion and mixing in porous media: Photobleaching pulse injection experiments and shear-enhanced mixing model. *Water Resources Research*, *53*(2), 1457-1472.

Karadimitriou, N. K. (2013). Two-phase flow experimental studies in micro-models (Doctoral dissertation, University Utrecht).

Karadimitriou, N. K., & Hassanizadeh, S. M. (2012). A review of micromodels and their use in two-phase flow studies. *Vadose Zone Journal*, *11*(3).

Karadimitriou, N. K., M. Musterd, P. J. Kleingeld, M. T. Kreutzer, S. M. Hassanizadeh, and V. Joekar-Niasar (2013), Water Resour. Res., 49, 2056–2067, doi:10.1002/wrcr.20196.

Karadimitriou, N. K., Joekar-Niasar, V., Babaei, M., & Shore, C. A. (2016). Critical role of the immobile zone in non-Fickian two-phase transport: A new paradigm. *Environmental science & technology*, *50*(8), 4384-4392.

Kohl, S. K., Landmark, J. D., & Stickle, D. F. (2006). Demonstration of absorbance using digital color image analysis and colored solutions. *Journal of Chemical Education, 83*(4), 644.

Korom, S. F. (1992). Natural denitrification in the saturated zone: a review. *Water resources research*, *28*(6), 1657-1668.

Lenormand, R., Touboul, E., & Zarcone, C. (1988). Numerical models and experiments on immiscible displacements in porous media. Journal of Fluid Mechanics, 189, 165-187. doi:10.1017/S0022112088000953

Lifton, V. A. (2016). Microfluidics: an enabling screening technology for enhanced oil recovery (EOR). *Lab on a Chip*, *16*(10), 1777-1796.

Mata A., Fleischman A.J., Roy S. (2005) Characterization of polydimethylsiloxane (PDMS) properties for biomedical micro/nanosystems. *Biomedical Microdevices*

Matyka, M., Khalili, A., & Koza, Z. (2008). Tortuosity-porosity relation in porous media flow. *Physical Review E*, *78*(2), 026306.

Nielsen, D. R., & Biggar, J. W. (1986). Water flow and solute transport processes in the unsaturated zone. *Water resources research*, *22*(9S).

Perestrelo, A. R., Águas, A. C., Rainer, A., & Forte, G. (2015). Microfluidic organ/body-on-a-chip devices at the convergence of biology and microengineering. *Sensors*, *15*(12), 31142-31170.

Pfannkuch, H. O., 1963. Contribution a l'étude des déplacement de fluides miscible dans un milieu poreux. *Rev. Inst. Fr. Petrol*, *18*(2), 215-270.

Preibisch, S., Saalfeld, S., Schindelin, J., & Tomancak, P. (2010). Software for bead-based registration of selective plane illumination microscopy data. *Nature methods*, *7*(6), 418.

Raoof, A., & Hassanizadeh, S. M. (2013). Saturation-dependent solute dispersivity in porous media: pore-scale processes. *Water Resources Research*, *49*(4), 1943-1951.

Rasband, W.S., ImageJ, U. S. National Institutes of Health, Bethesda, Maryland, USA, https://imagej.nih.gov/ij/, 1997-2016.

Rose, D. A. (1973). Some aspects of the hydrodynamic dispersion of solutes in porous materials. *European Journal of Soil Science*, *24*(3), 284-295.

Saffman, P.G. & Taylor, G. (1958). The penetration of a fluid into a porous medium or Hele-Shaw cell containing a more viscous liquid. *Proc. Roy. Soc. London A,* 245, 312-329.

Sahimi, M., Hughes, B. D., Scriven, L. E., & Davis, H. T. (1986). Dispersion in flow through porous media—I. One-phase flow. *Chemical engineering science*, *41*(8), 2103-2122.

Sayegh, S. G., & Fisher, D. B. (2008, January). Enhanced oil recovery by CO flooding in homogeneous and heterogeneous 2D micromodels. In *Canadian International Petroleum Conference*. Petroleum Society of Canada.

Shen, L., & Chen, Z. (2007). Critical review of the impact of tortuosity on diffusion. *Chemical Engineering Science*, *62*(14), 3748-3755.

Toride, N., F. J. Leij, and M. Th. van Genuchten, The CXTFIT code for estimating transport parameters from laboratory or field tracer experiments. Version 2.0, Research Report No. 137, U. S. Salinity Laboratory, USDA, ARS, Riverside, CA, 1995.

Vitousek, P. M., Aber, J. D., Howarth, R. W., Likens, G. E., Matson, P. A., Schindler, D. W., ... & Tilman, D. G. (1997). Human alteration of the global nitrogen cycle: sources and consequences. *Ecological applications*, *7*(3), 737-750.

Vörösmarty, C. J., Green, P., Salisbury, J., & Lammers, R. B. (2000). Global water resources: vulnerability from climate change and population growth. *science*, *289*(5477), 284-288.

Wan, J., & J. L. Wilson (1994), Colloid transport in unsaturated porous media, *Water Resour. Res.*, 30(4), 857–864, doi:10.1029/93WR03017.

Xu, M., & Eckstein, Y. (1997). Statistical analysis of the relationships between dispersivity and other physical properties of porous media. Hydrogeology Journal, 5(4), 4-20.

Zentner, E., Gerstl, Z., Weisbrod, N., Lev, O., Pankratov, I., Russo, D., ... & Ronen, D. (2015). Deep penetration of pharmaceuticals and personal care products through the vadose zone of effluent-irrigated land. *Vadose Zone Journal*, *14*(1).

Zhang, Q., Hassanizadeh, S. M., Karadimitriou, N. K., Raoof, A., Liu, B., Kleingeld, P. J., & Imhof, A. (2013). Retention and remobilization of colloids during steady-state and transient two-phase flow. *Water Resources Research*, *49*(12), 8005-8016.

Zhang, Q., Raoof, A., & Hassanizadeh, S. M. (2015). Pore-scale study of flow rate on colloid attachment and remobilization in a saturated micromodel. *Journal of environmental quality*, *44*(5), 1376-1383.

Zhao, C. X. (2013). Multiphase flow microfluidics for the production of single or multiple emulsions for drug delivery. *Advanced drug delivery reviews*, *65*(11), 1420-1446.